minerals

MDPI

Review

Nanocrystalline Principal Slip Zones and Their Role in Controlling Crustal Fault Rheology

Berend A. Verberne [1,*], Oliver Plümper [2] and Christopher J. Spiers [2]

[1] Geological Survey of Japan, National Institute of Advanced Industrial Science and Technology, 1-1-1 Higashi, Tsukuba, Ibaraki 305-8567, Japan

[2] Department of Earth Sciences, Utrecht University, P.O. Box 80.021, 3508 TA Utrecht, The Netherlands; o.plumper@uu.nl (O.P.); c.j.spiers@uu.nl (C.J.S.)

* Correspondence: ba.verberne@aist.go.jp; Tel.: +81-29-861-5211

Received: 7 May 2019; Accepted: 25 May 2019; Published: 28 May 2019

Abstract: Principal slip zones (PSZs) are narrow (<10 cm) bands of localized shear deformation that occur in the cores of upper-crustal fault zones where they accommodate the bulk of fault displacement. Natural and experimentally-formed PSZs consistently show the presence of nanocrystallites in the <100 nm size range. Despite the presumed importance of such nanocrystalline (NC) fault rock in controlling fault mechanical behavior, their prevalence and potential role in controlling natural earthquake cycles remains insufficiently investigated. In this contribution, we summarize the physical properties of NC materials that may have a profound effect on fault rheology, and we review the structural characteristics of NC PSZs observed in natural faults and in experiments. Numerous literature reports show that such zones form in a wide range of faulted rock types, under a wide range of conditions pertaining to seismic and a-seismic upper-crustal fault slip, and frequently show an internal crystallographic preferred orientation (CPO) and partial amorphization, as well as forming glossy or "mirror-like" slip surfaces. Given the widespread occurrence of NC PSZs in upper-crustal faults, we suggest that they are of general significance. Specifically, the generally high rates of (diffusion) creep in NC fault rock may play a key role in controlling the depth limits to the seismogenic zone.

Keywords: nanograins; principal slip zone; crystallographic preferred orientation; amorphization; mirror-slip surface; faults; earthquakes; localization

1. Introduction

Nanocrystalline materials are widespread in the Earth's atmosphere, biosphere, and in the subsurface [1–5], including in principal slip zones (PSZs) within natural faults [6–8]. PSZs are zones of localized shear deformation that (have) accommodate(d) the bulk of displacement in the cores of upper-crustal faults [9,10], which suggests that the physical properties of the ultrafine(nano)-grained fault rock within PSZs plays an important role in controlling fault mechanical behavior or fault rheology. From observations on metals and ceramics it is well known that nanophase materials, characterized by grain sizes < 100 nm, frequently exhibit unusual deformation properties compared with coarser-grained counterparts [11–13]. The reason for this is the loss of cohesive energy between atoms comprising the grain as its size continues to decrease. In view of the generality of this nanograin size effect, it is important to consider the potential physical implications of nanogranular fault rock. Despite the emerging awareness on the importance of nanophase geomaterials in Earth sciences [1–8], their prevalence in upper-crustal faults and potential role in natural earthquake cycles remains insufficiently investigated.

In this paper, we aim to elucidate the significance of nanocrystalline PSZs in Earth's upper crust. We start with background on fault mechanics and upper-crustal seismogenesis, and summarize some key physical properties of nanophase materials which, when applied to fault rock, are expected to be of major importance in controlling fault strength and stability. We go on to review the micro- and nanostructural characteristics of natural and experimentally-formed nanocrystalline PSZs, and list reports from the literature of PSZs characterized by grains <100 nm in size. Our work demonstrates that nanocrystalline PSZs form under a wide range of conditions pertaining slow (a-seismic) and fast (co-seismic) upper-crustal fault slip. Also, we observe that they are frequently characterized by an internal crystallographic preferred orientation, and by the presence of amorphous materials and/or glossy fault plane interfaces known as "mirror-slip" surfaces. Given the abundant observations of nanocrystalline PSZs in field exposures of faults, as well as in experiments, we suggest that they are of general importance to upper-crustal fault deformation. The physical properties of nanocrystalline fault rock may play a key role in natural earthquake cycles, especially in controlling the depth distribution of upper-crustal seismicity.

2. Fault Zones, Earthquakes, and the Seismogenic Zone

The presence of long-lived, localized zones of shear deformation in the crust, or fault zones, implies that the fault rocks within are weaker than the surrounding country rocks and that their weakness is persistent [14,15]. The strength of the upper-crust is classically approximated using a Coulomb-type, brittle failure law, abruptly giving way to ductile deformation below ~15 to 20 km depth (Figure 1a) [16,17]. A brittle-to-ductile transition at ~15 to 20 km depth is consistent with geological and seismological observations of the base of the so-called "seismogenic zone", i.e., the depth interval in the upper-crust in which the bulk of upper-crustal earthquakes nucleate [18–25], suggesting that at greater depths earthquake rupture nucleation is inhibited by intrinsically stable, ductile or viscous flow in shear zones. A seismicity cut-off at shallower depths, typically observed at ~2–4 km, demarcates the upper limit of the seismogenic zone [24,26]. Field and laboratory studies of fault deformation suggest that within the seismogenic zone, "multi-mechanism" or "frictional-viscous" fault slip-involving coincident rate-sensitive (creep) and rate-insensitive (e.g., cataclasis) deformation mechanisms-plays an important role (Figure 1b) [27–37]. However, in general, the microphysical processes responsible for aseismic fault sliding above the seismogenic zone, and for seismogenic slip within, remain poorly understood for most fault rock types.

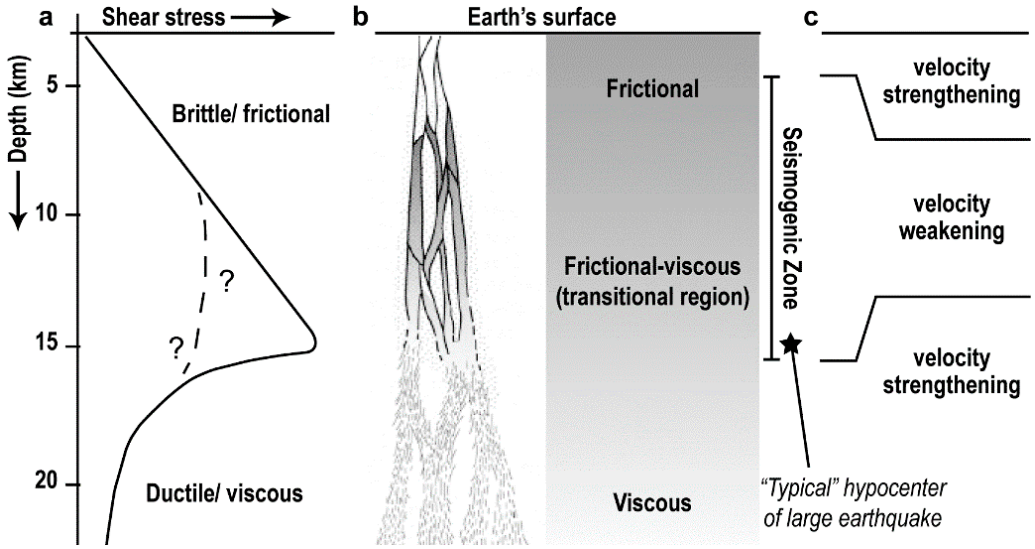

Figure 1. Schematic profile of a fault zone in Earth's upper-crust. (**a**) Fault strength vs. depth. (**b**) Fault zone sketch (from [15]), with a rough depth range indicating fault deformation regimes, the seismogenic zone, and (**c**) velocity dependence or intrinsic fault stability regimes.

In the case of earthquakes, sliding along faults is achieved by unstable, periodic slip events instead of by stable, continuous motion. This is similar to the jerky sliding motion that is frequently observed in laboratory rock friction experiments, known as "stick-slip" [38]. Regular stick-slip behavior can be easily envisioned using a spring-block model system, consisting of a rigid block or slider on a nominally flat surface, driven via a spring of a certain stiffness. When the spring is pulled at constant speed, an instability may develop depending on the frictional properties of the slider-surface contact, the mass of the block, the spring stiffness, and the loading rate, resulting in intermittent slider acceleration and stationary contact [39–42]. Ruina [41] showed that for regular stick-slip to occur the slider-surface contact must decrease in strength with increasing displacement rate, hence be "velocity-weakening". In the opposite case "velocity-strengthening" occurs, which leads to a state of stable sliding [41,43]. Thus, the seismogenic zone is believed to represent a depth interval in the upper-crust where shear deformation of fault zones leads to unstable, velocity-weakening behavior, as opposed to stable velocity-strengthening above and below (Figure 1c) [22,24,25,44].

Importantly, the velocity dependence of frictional strength is a material property of the sliding medium which constitutes the slider-surface contact. Applying this to natural faults, the sliding medium is represented by the granular wear product of cumulative slip along the fault, or "fault gouge", present in the fault core [45]. Field and drilling studies of active and inactive natural fault zones frequently demonstrate the presence of a mm- to cm-wide principal slip zone (PSZ) in the gouge-filled fault core that accommodates, or has accommodated, the bulk of displacement along the fault [9,46–52]. Tectonic loading of a faulted rock volume, as occurs continuously in numerous geologic settings (e.g., at tectonic plate boundaries), causes energy dissipation predominantly along the PSZ [10,53]. In the case of slow (aseismic) fault sliding, quasi-static deformation of fault rock is believed to be key [54–56], whereas at higher (seismic) slip rates frictional heat generated along the PSZ plays an increasingly important role [57], leading to dynamic fault rupture processes such as melting, decarbonation, and/or thermal pressurization [58–63].

3. The Physical Properties of Nanophase Materials

Material properties such as melting temperature or yield point frequently show drastic changes when the grain size decreases to the nanometer-realm (<100 nm) [11–13]. The reason for this is fundamental; a decreasing grain size implies a parabolic increase of the fraction of surface atoms (Figure 2a), which have a much lower average binding energy compared with atoms in the bulk phase. This means that when the grain size decreases to that of a few atoms or unit cells, it has major implications for thermodynamic stability and reactivity of the individual particles [64–66]. For example, the melting point of Au particles is observed to decrease from ~1300 K to 700 K as the grain size decreases from 20 nm to 5 nm [67] (Figure 2b). Observations on common rock-forming minerals are scarcer. However, in the case of calcite, which is the dominant constituent of limestone, the decomposition temperature decreases from ~1075 K to 950 K as the grain size decreases from 40 nm to 20 nm [68] (Figure 2b). Size-dependence of the melting or decomposition temperature of fault rock within a principal slip zone (PSZ) may have major implications for bulk fault rheology, for example at elevated temperatures due to frictional heating.

Another unique aspect relevant to nanostructured polycrystals and fault rock is their huge cumulative grain surface area, which naturally increases exponentially as the grain size continues to decrease (Figure 2c). This has major implications not only for chemical reactivity but also for the rheology of a material. For example, due to the short grain scale transport distances in nanostructured materials [69], grain boundary diffusion driven mechanisms [70–72] are generally fast, enabling superplastic deformation at much lower temperatures/higher strain rates than compared with in coarser-grained materials [73–75]. The high grain boundary density also plays an important role in dislocation-mediated plasticity. As the grain size decreases to the <100 nm size range, dislocations are emitted and adsorbed efficiently at grain boundaries, leading to a decrease of the material yield strength with decreasing grain size hence an "inverse Hall-Petch effect" [76–79] (Figure 2d). In this

mechanism, dislocations traverse the crystallite within very brief time windows, achieving very large strains while leaving a micro-/nanostructure characterized by "strain-free" nanograins [80–82].

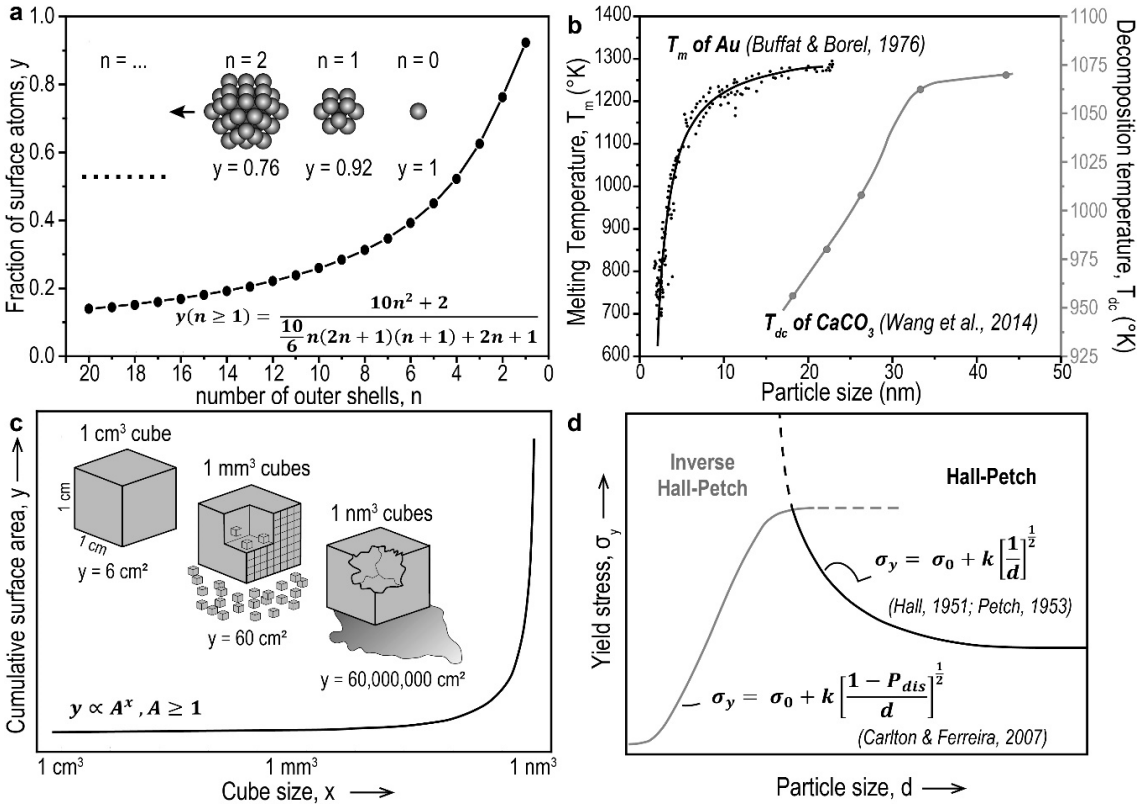

Figure 2. Key characteristics of nanoparticles and nanostructured materials. (**a**) A simple model of hexagonal close-packed balls illustrating the effect of particle miniaturization. The fraction of surface particles increases near-exponentially with decreasing number of outer shells, or particle size (after [11,13]). (**b**) The melting temperature of Au [67] and the decomposition temperature of $CaCO_3$ [68] particles decrease sharply as particle size decreases within the nm-realm. (**c**) The cumulative surface area of polycrystals increases exponentially as the grain size continues to decrease. (**d**) The empirical relation between yield strength σ_y and grain size d, known as the Hall-Petch (HP) effect [76,77], reverses for very small d (after [78,79]). The expression for σ_y in the inverse-HP regime is the model by Carlton & Ferreira (2007) [79], where k is a constant and P_{dis} is the probability of a dislocation being absorbed by a grain boundary.

4. Nanocrystalline Principal Slip Zones in Natural Faults and in Experiments

Observations of natural and experimentally-formed principal slip zones (PSZs) showing the presence of <100 nm-sized grains are listed in respectively Tables 1 and 2. Below we summarize the micro- and nanostructural characteristics of nanocrystalline PSZs, highlighting seminal reports of field/drilling studies of natural faults and of laboratory studies. Much insight was obtained recently from studies of glossy or "mirror-like" fault slip surfaces (MSSs) formed in experimentally simulated faults composed of calcite fault gouge. These are described using a separate section. While we aspire to provide as complete an overview as possible, we may have overlooked some of the studies performed to date.

4.1. Nanocrystalline Principal Slip Zones in Exposures of Natural Faults

Faults that are exposed in an orientation normal to the fault plane display a cross-section through the damage zone that has developed upon repeated fault displacement, including the principal slip zone(s) (Figure 3a). Power and Tullis [83] used optical and transmission electron microscopy (TEM)

to investigate sections prepared normal to the fault plane of rocks collected from the glossy fault trace of the Dixie Valley thrust fault (USA). In a zone just ~0.2 mm wide, the fault trace or PSZ is characterized by ultrafine grains down to 10 nm in size, and a uniform optical birefringence and extinction. This optical effect may be observed in (ultra)thin sections using crossed nicols in a polarizing light microscope (by rotating the microscope stage as shown in Supplementary Video S1) and is widely used as indicative of a crystallographic preferred orientation (CPO). Chester & Goldsby [84] also reported a nanocrystalline PSZ with a CPO, in fault core samples from the Punchbowl Fault (USA). Field investigation revealed visually distinct, 0.15 to 0.55 m thick layers of fine-grained fault gouge known as ultracataclasite, separated by what was identified as a "principal fracture surface" [46]. However, thin section analyses revealed that the ultracataclasite layers were separated by a zone of finite width (constituting a principal slip *zone*), characterized by a strong uniform birefringence, and the presence of grains down to 4 nm in size [7,84]. Other notable observations of naturally-formed nanocrystalline PSZs have been made from drilling of seismically-active fault zones, such as the Chelungpu Fault (Taiwan) [8,85] and the San Andreas Fault (USA) [86].

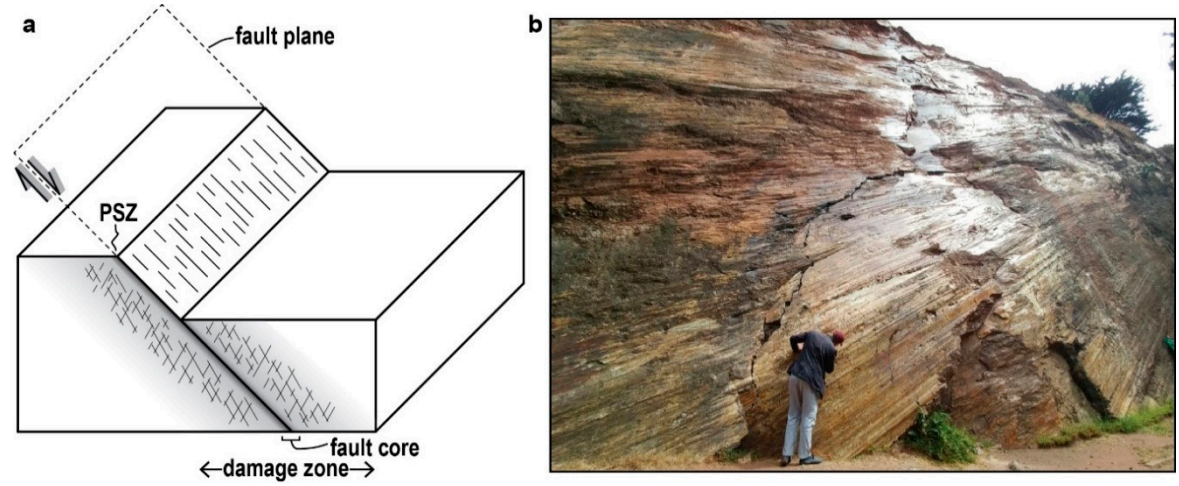

Figure 3. Principal slip zones (PSZs) in natural faults. (**a**) Sketch of a normal fault, highlighting the fault plane, damage zone, fault core, and PSZ (after [10,47]). (**b**). Striated, glossy surface of the Corona Heights Fault (USA) (courtesy of J. E. Samuelson).

Faults that are exposed parallel to the fault plane display the fault core, which is frequently characterized by slip-parallel striations and a relatively erosion-resistant, "glossy" or "well-polished" surface (Figure 3b) (Table 1). Such exposures have been reported as meter-scale outcrops in the field [87,88], but also as cm-scale patches in drill core samples of active faults [85,86]. Siman-Tov et al. [87] coined the term "fault mirrors" for highly light-reflective fault surfaces cutting carbonate rocks in the Dead Sea transform region (Israel). They showed that the glossy fault plane is internally composed of a thin (<1 μm) veneer of calcite grains of a size down to ~50 nm. However, a glossy or mirror-like appearance has been described for fault surfaces composed of 0.1–1 μm-sized grains [85,89,90], and do not reveal much about the grain size within. As pointed out by Siman-Tov et al., the specular reflectivity occurs because the fault surface roughness has a wavelength shorter than that of visible light (400 nm) [91].

Another notable observation that has been frequently reported on using samples from naturally occurring nanocrystalline PSZs is the presence of (partly) amorphized material (Table 1). It may be observed as cm-thick veins in the field [92], or as thin coatings surrounding mineral clasts when observed using TEM [86,93,94]. Veins of glassy, amorphized rock known as pseudotachylytes, may form as a result of frictional melting along faults, pointing to high (co-seismic) slip rates [45,95,96]. For this reason, melt-origin pseudotachylytes are frequently used as field indicators of paleo-earthquake rupture [97,98]. However, the formation process is not implicit to the definition of pseudotachylytes,

and they may form by other mechanisms than seismically-induced frictional melting [99]. Caution is necessary on the interpretation of field exposures of faults showing the presence of amorphous veins.

Table 1. List of reports, in chronological order, of ≤100 nm-sized grains in the cores (principal slip zones) of natural faults.

Location	Dominant Host Rock Mineralogy	*d* (nm)	CPO?	Glossy Surface?	Amorphous Material?	Source
Dixie Valley Thrust, USA	quartz	10	√	√		Power & Tullis [83]
Punchbowl Fault, USA	quartz, feldspar, clays	4	√			Chester & Goldsby [84]
Chelungpu Fault (TCDP borehole C)	quartz, clays	50				Ma et al. [8]
Nojima Fault Zone, Japan	quartz, feldspar	30				Keulen et al. [100]
Iida-Matsukawa Fault, Japan	quartz, feldspar	20			√	Ozawa & Takizawa [92]
San Andreas Fault (SAFOD main hole)	clays, quartz, feldspar	50		√	√	Janssen et al. [86]
Kfar Gladi Fault, Israel	calcite	50		√		Siman-Tov et al. [87]
Corona Heights Fault, USA	silica, quartz	10	√	√	√	Kirkpatrick et al. [88]
Gubbio Fault, Italy	calcite, clays	50		√		Bullock et al. [101]
Mt. Maggio fault, Italy	calcite	100				Collettini et al. [102]
Vado di Corno fault, Italy	calcite, dolomite	50		√		Demurtas et al. [103]
Capolivieri-Porto Azurro shear zone, Italy	tourmaline	10–100 †			√	Viti et al. [90]
Hsiaotungshi fault system (borehole), Taiwan	quartz, clays	50–100		√	√	Kuo et al. [85]
Maclure Glacier, USA	feldspar, quartz	10–100		√	√	Siman-Tov et al. [104]
Mt. Vettore Fault, Italy	calcite, clays	50		√		Smeraglia et al. [105]

"*d*" is the minimum grain size observed. † Fault mirrors (glossy surfaces) are also reported, however here they are composed mainly of >200 nm sized crystals. See the respective papers for details on localities, outcrops, and PSZ formation conditions.

4.2. Nanocrystalline Principal Slip Zones Formed in Fault-Slip Experiments

Laboratory experiments aiming to investigate upper-crustal fault deformation are carried out by imposing displacement along (initially) bare rock surfaces, or on a powdered sample layer representing a simulated fault gouge. The technology used to conduct fault-slip experiments varies greatly [106–108]. However, for simplicity, here we distinguish between two types of fault-slip tests; (i) low-velocity friction (LVF) tests, used to study slow fault-slip including the early (nucleation) stages of earthquake rupture, and (ii) high-velocity friction (HVF) tests, used to study dynamic earthquake rupture processes. Following Rowe & Griffith [98], slip rates (v) beyond ~10^{-4} m/s are "almost certainly dynamic", so we define HVF tests as using $v \geq 10^{-4}$ m/s, and LVF tests as using $v < 10^{-4}$ m/s. There are numerous other differences between LVF and HVF tests, in addition to the displacement rate used, that may affect micro- and nanostructural development along the simulated fault, or its recovery after an experiment. LVF tests typically achieve steady-state conditions of normal stress (σ_n) and temperature (T), but reaching cumulative displacements of maximally a few centimeters ($\sum x = 10^{-3}$–10^{-2} m). HVF tests may run for meters ($\sum x = 10^{1}$–10^{2} m), with frictional heat generated at the fault-slip interface playing an important role.

Despite the major differences between LVF and HVF tests, simulated fault samples recovered after an experiment typically show one or more, ultrafine-grained, shear plane-parallel bands of finite width, located in the sample interior ("Y-shears") or close to the loading piston interface ("boundary shears") [109,110] (Figure 4a–d). These shear bands mark a zone of abrupt grain size reduction with respect to the host rock (Figure 4b,d), and accommodated the bulk of the imposed shear displacement, i.e., representing experimentally-formed principal slip zones (PSZs). PSZ thicknesses may range from ~50–100 μm in samples recovered from LVF tests, to a few (tens of) microns in HVF deformed samples. Yund et al. [111] used TEM to investigate PSZs developed in simulated fault gouges of siliceous and carbonate compositions deformed in LVF and HVF rotary shear tests (Table 2). They reported grain sizes down to ~10–50 nm in all samples investigated, and the presence of amorphized materials, except in the carbonates. However, there are numerous (recent) reports of nanocrystalline PSZs formed in

LVF and HVF experiments using simulated fault samples composed of carbonates [58,93,112–119], many of which also showed the presence of amorphous materials (Table 2).

A crystallographic preferred orientation (CPO) was reported for nanocrystalline PSZs developed in LVF tests using simulated gouges composed of calcite [113,114,118] and quartz [120] (Table 2). The presence of a CPO may be inferred from uniform birefringence and extinction observed in thin sections (Supplementary Video S1), or else demonstrated using selected area diffraction in TEM. Electron backscatter diffraction is a powerful tool frequently used to quantify a CPO [121], however, to our knowledge this remains difficult to apply to extremely fine-grained aggregates such as those characterizing nanocrystalline PSZs (grain size << 100 nm). Recently, EBSD measurements were used to quantify a CPO characterizing a PSZ composed of 200–300 nm-sized, polygonal grains, formed in simulated calcite gouge sheared in HVF tests [122,123].

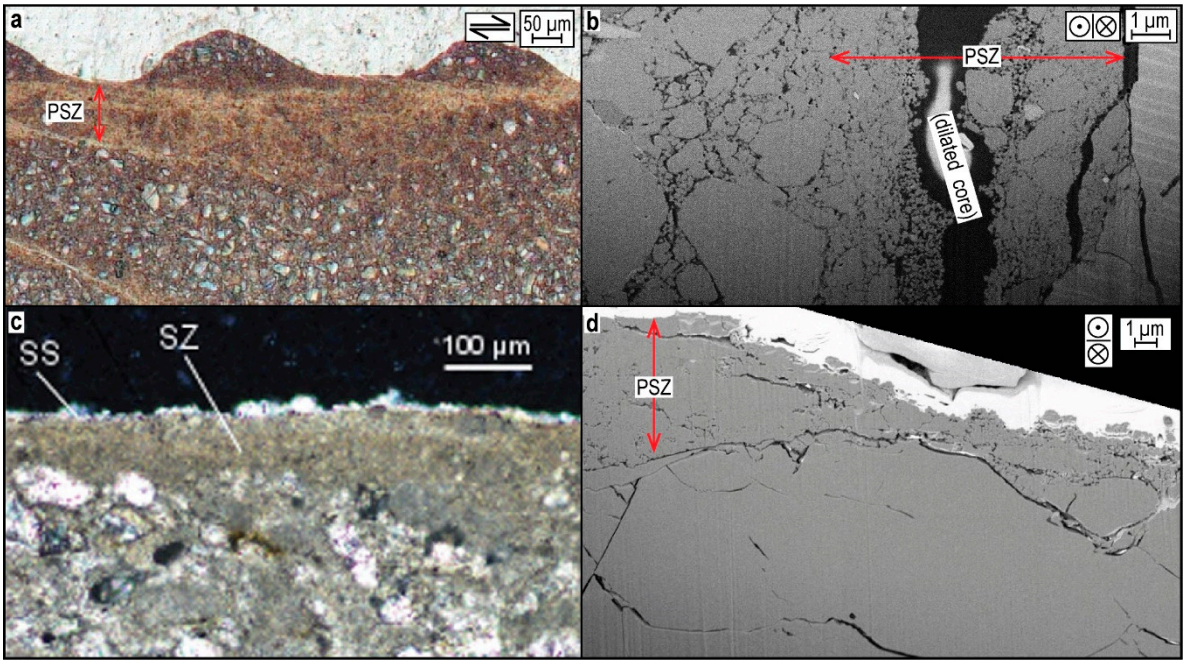

Figure 4. Principal slip zones (PSZs) in simulated calcite(-rich) fault gouge formed in LVF (**a**,**b**) and HVF experiments (**c**,**d**). (**a**) Plane polarized light micrograph of an ultra-thin section (parallel to the slip vector, sample $CaCO_3$-RT-dry of [113]). (**b**) Backscatter electron (BSE) micrograph prepared using a focused ion beam scanning electron microscope (FIB-SEM) (normal to the slip vector, sample lmst@150 °C of [124]). The central void is due to post-test dilation. (**c**) Cross-polarized light micrograph showing a narrow, fine-grained slip zone (SZ) bound by a slip surface (SS). Taken with publisher's permission from [93]. (**d**) BSE micrograph. Taken from [115].

Table 2. List of reports, in chronological order, of <100 nm-sized grains in experimentally-formed principal slip zones.

Dominant Sample Mineralogy	v_{max} (m/s)	σ_n (MPa)	$\sum x$ (m)	d (nm)	CPO?	Glossy Surface(s)?	Amorphous Material?	Source
quartz	10^{-5}	~135	10^{-5}	90			√ †	Engelder [125]
quartz	$10^{-2.5}$	7–50	10^{-1}	10–15			√	Yund et al. [111]
quartz, feldspar	$10^{-2.5}$–10^{-6}	50–75	10^{-2}–10^{-1}	10–15			√	Yund et al. [111]
calcite	$10^{-2.5}$	15	10^{-2}	~50				Yund et al. [111]
dolomite	$10^{-2.5}$	75	10^{-1}	~50				Yund et al. [111]
calcite	10^{-2}–10^{0}	1.1–13.4	10^{0}–10^{1}	10		√		Han et al. [58]
siderite, magnetite	10^{0}	0.6–1.3	10^{1}	20–30		√		Han et al. [112]
antigorite	10^{0}	24.5	10^{0}	~50			√	Viti & Hirose [126]
quartz, feldspar	10^{-7}–10^{-8}	>10^{3}	10^{-3}	8		√	√	Pec et al. [127,128]
calcite	10^{-7}–10^{-5}	50	10^{-3}	5	√	√	√ ††	Verberne et al. [113,114]
dolomite	10^{0}	28.4	10^{-1}	10		√		Green II et al. [116]
quartz, feldspar	10^{-6}–10^{-5}	25	10^{-2}–10^{-1}	15–50			√	Hadizadeh et al. [129]
quartz, clays	10^{0}	1	10^{1}	10–50			√	Kuo et al. [130]
quartz, silica	10^{-6}	>10^{3} †	10^{-3}	5	√		√	Toy et al. [120]
calcite	10^{-1}–10^{0}	10	10^{-3}–10^{1}	5–10		√	√	Spagnuolo et al. [115]
calcite	10^{-1}	0.47–1.57	10^{1}	45		√		Siman−Tov et al. [117]
quartz	10^{-7}–10^{-3} ‡	92–287	10^{-3}	10		√	√	Hayward et al. [131]
quartz, smectite	10^{-4}–10^{0}	5	10^{0}	10–50			√	Aretusini et al. [132]
quartz, muscovite	10^{-8}–10^{-5}	120	10^{-4}	10	√			Niemeijer [133]
quartz, muscovite	10^{-4}	120	10^{-4}	10	√			Niemeijer [133]
calcite	10^{-7}–10^{-5}	20–100	10^{-3}–10^{-4}	10				Mercuri et al. [119]
calcite	10^{-6}–10^{-5}	45	10^{-1}–10^{-2}	50	√		√	Delle Piane et al. [118]
quartz	10^{-4}–10^{-1}	2.5–5	10^{0}–10^{1}	10		√	√	Rowe et al. [134]

Grey shaded rows include data from LVF tests (here defined as tests employing $v < 10^{-4}$ m/s). v_{max} = max. displacement rate; σ_n = (effective) normal stress; $\sum x$ = accumulated displacement; d = min. grain size. Only the orders of magnitude of v_{max} and $\sum x$ are given. Glossy surfaces refer to the presence of "shiny" or "mirror-like" surfaces, regardless of continuity. For details see the respective literature. † Attributed to beam damage. †† Attributed to unknown contamination. ‡ v_{max} here was estimated from unstable slip events.

Mirror-Slip Surfaces in Principal Slip Zones Developed in Calcite Gouge

"Glossy", "shiny", or "mirror-like" slip surfaces (MSSs) have been observed in experiments using a wide range of sample materials, characterized by a wide range of normal stresses (σ_n), displacement rates (v), and cumulative displacements ($\sum x$) (Table 2) (Figures 5 and 6). Recently, much attention has been given to MSSs developed in simulated faults composed of calcite, mainly because of their striking similarity with carbonate "fault mirrors" frequently observed in tectonically-active carbonate terrains [87,135], and the question whether they may be indicators of past seismic slip.

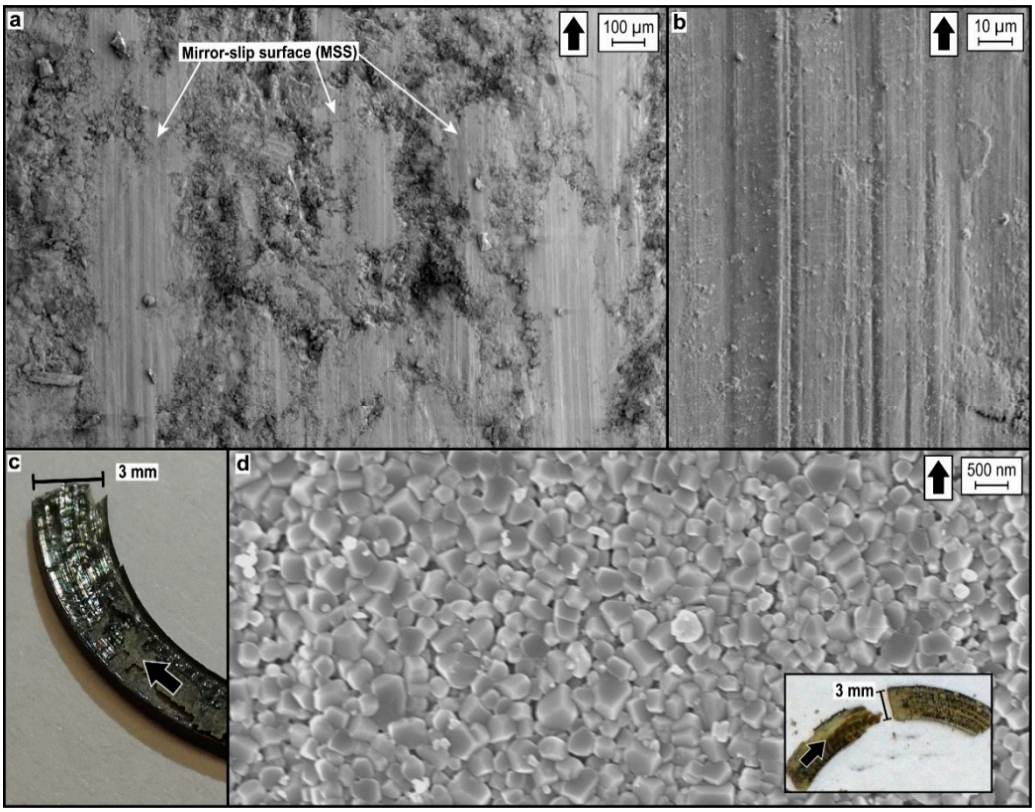

Figure 5. Principal slip zones with mirror-slip surfaces formed in simulated calcite gouge sheared in HVF tests ($v \geq 10^{-4}$ ms^{-1}). (**a**,**b**) Secondary electron (SE) micrographs. From [115]. (**c**) Sample fragment recovered from an experiment conducted using $0.1 \leq v \leq 100$ µms^{-1}, $\sigma_n^{eff} = 50$ MPa, $T = 550$ °C, $\sum x = 24.7$ mm (unpublished data). (**d**) Top view onto the PSZ developed in an experiment conducted at $v = 100$ µms^{-1} (sample $CaCO_3$-550-vhigh of [122]). Inset shows a photo of the (fragmented) sample recovered after the experiment.

In general, MSSs are characterized by extremely low surface roughness, especially in a direction parallel to the shear direction [136,137]. They have been reported as multiple, elongated patches aligned parallel to the shear direction (Figures 5a and 6a), or else as a single, continuous interface marking the PSZ boundary (Figure 5c). The number and extent of MSSs were shown to increase with increasing displacement and/or displacement rates, in HVF tests conducted at normal stresses up to 26 MPa [117,135,138], which led some authors to conclude that continuous MSSs may indeed serve as indicators of past seismic slip in natural faults cutting carbonates. However, a continuous MSS has also been observed in simulated calcite gouge sheared at $v = 10$ µms^{-1} (effective normal stress 20 MPa $\leq \sigma_n^{eff} \leq 100$ MPa, $T \approx 550$ °C, $\sum x = 12.4$ mm; Figure S2D of [122]). The role of effective normal stress, and of cumulative displacement, on the formation of (patchy) MSSs with progressive shear strain in LVF tests remains to be investigated. Pozzi et al. [139] recently reported on the microstructural development of MSS-bearing PSZs with progressive shear strain in HVF experiments on simulated calcite faults ($\sigma_n = 25$ MPa, v up to 1.4 m/s). Using polished sections prepared normal to the slip vector

they observed that, after an initial stage of slip ($\Sigma x \approx 7$ cm), sharp discontinuities develop which are interpreted to represent MSSs. The matured PSZ is observed to consist of 200–300 nm sized, polygonal grains characterized by a crystallographic preferred orientation [123].

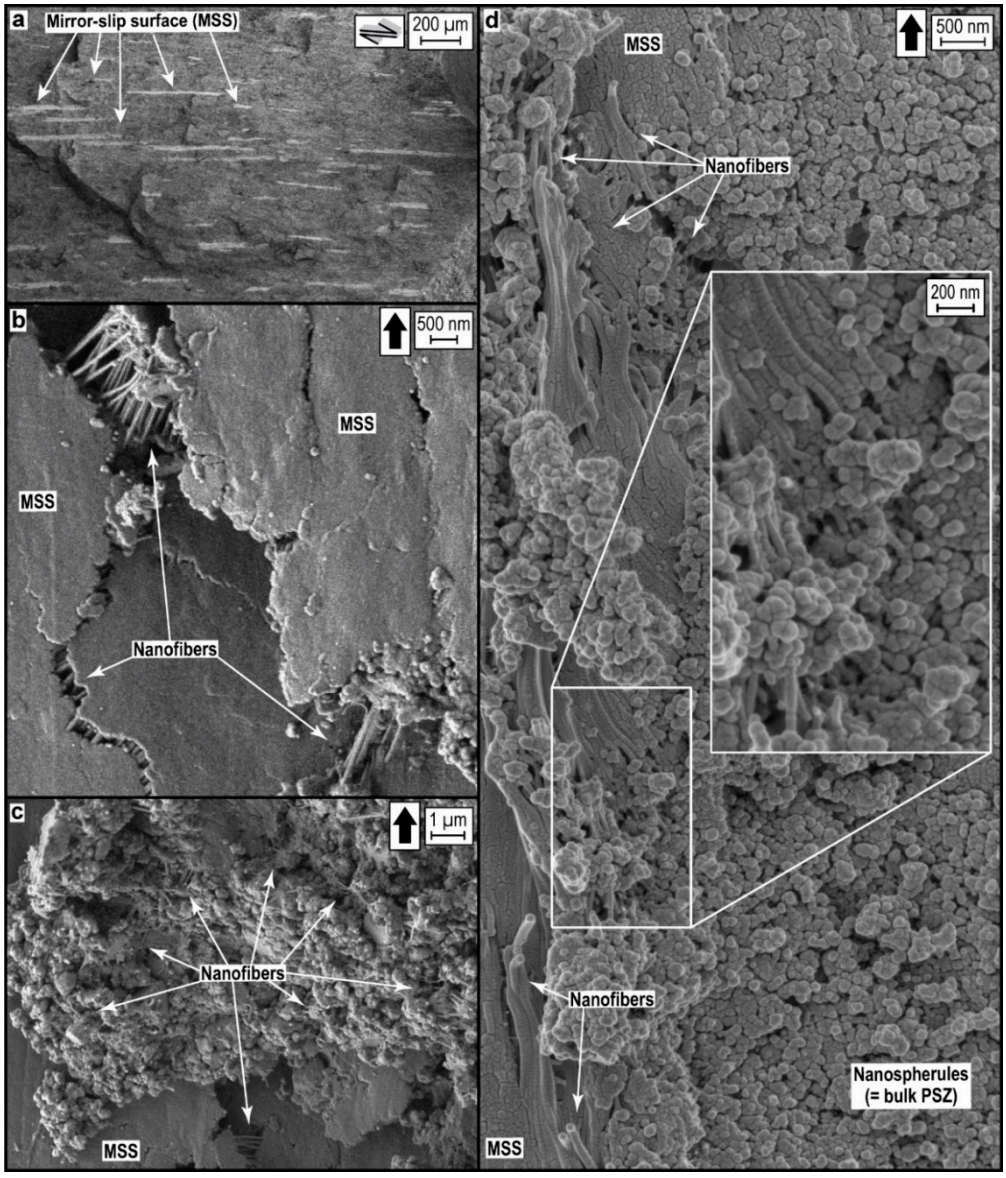

Figure 6. Principal slip zone with mirror-slip surfaces formed in simulated calcite gouge sheared in LVF tests ($v = 10^{-6}$ to 10^{-5} ms^{-1}, see [140]). Secondary electron micrographs. (**a**) Taken at an angle of 52° to the shear plane. The patches that are elongated parallel to the shear direction represent MSSs. (**b**) Stretched nanofibers and (**c**) nanofibers within the bulk PSZ. (**d**) Alignment of nanospherules at the edge of an MSS. (a) to (d) are top views onto the shear plane. The micrographs shown in (**a**,**d**) are from sample SEMB of [140], taken using a FEI Nova Nanolab FIB-SEM. The micrographs in (**b**,**c**) are of samples sheared using a gas-medium deformation apparatus installed at the Geological Survey of Japan (Tsukuba, Japan), and taken using a JEOL-7400F FEG-SEM.

Returning to patchy MSSs formed in LVF experiments using calcite gouge ($v = 10^{-6}$ m/s, $\sigma_n^{eff} = 50$ MPa, $\sum x \approx$ 5–6 mm), individually these show remarkable micro- and nanostructural characteristics (Figure 6a–d) [140]. The PSZ itself comprises a porous, sheet-like volume of ~100 nm-sized spherical particles, with internal, 0.1 to 1 µm-thick, dense planar coatings comprising the MSSs. The MSS patches are observed at different topographic levels within the PSZ (Figure 6a) and are internally

composed of ~100 nm wide fibers that show marked extension and plastic bending when stretched (Figure 6b–d). At locations where stretching led to nanofiber failure, necking structures are absent, suggestive of a low stress-sensitivity of the ductile strain rate (a low "*n*-value"), or superplastic behavior [140]. Nanofiber stretching in this way could only have occurred upon opening of the microcracks at room conditions after the experiment. The nanofibers are locally observed away from MSSs, i.e., within the porous volume constituting the broader PSZ (Figure 6c). Selected area diffraction patterns, taken using TEM, of a single nanofiber as well as of the spherical particles comprising the bulk PSZ, revealed a polycrystalline substructure composed of crystallites 5 to 20 nm in size, characterized by a CPO [113,114,140]. The uniform width of the nanofibers and the spherical nanograin aggregates or nanospherules, (both with diameter ~100 nm), combined with the alignment observed of nanospherules at the edge of some MSSs (Figure 6d), suggest that the nanofibers represent linear nanospherule chains.

5. Discussion

The compilation of literature observations reported above (Tables 1 and 2) demonstrates that nanocrystalline principal slip zones (NC PSZs) form in a wide range of rock types under a wide range of normal stresses and displacement rates pertaining to co-seismic and sub-seismic fault-slip in Earth's upper-crust. This suggests that NC PSZs play an important role in controlling fault sliding behavior, including earthquake rupture nucleation and dynamic propagation. Below we discuss possible formation mechanisms of the PSZ nanostructures observed, as well as a comparison between mirror-slip-surface-bearing PSZs developed in low-velocity friction (LVF; $v < 10^{-4}$ ms^{-1}) and in high-velocity friction (HVF; $v \geq 10^{-4}$ ms^{-1}) tests. We go on to discuss the role of NC PSZs in controlling upper-crustal fault strength and stability, and we consider their broader significance in the seismogenic zone.

5.1. Formation of PSZ Nanostructures, Amorphous Materials, and CPO

Under brittle conditions in a fault zone, grain size reduction occurs by cataclastic deformation involving intragranular fracture, comminution and intergranular friction [100,141–143]. However, below a certain critical grain size d_{crit} known as the grind limit, the stress required to initiate a fracture in compression becomes too high so that plastic yielding occurs [144]. For quartz, $d_{crit} \approx 0.9$ μm [100], whereas for calcite $d_{crit} \approx 0.85$ μm [145]. This means that the <100 nm-sized grains frequently observed in fault-slip experiments must point to a mechanism of grain size reduction involving plastic yielding. Using a model based on mode I Griffith failure [144,146] and low-temperature plasticity, Sammis and Ben-Zion [147] showed that in the case of quartz in a compressive regime, shock loading and subcritical crack growth may produce particles down to 3 nm in size. However, specifically for LVF experiments which employ displacement rates of μm/s and reach just millimeters of cumulative displacement over the timespan of a few hours, the formation of crystallites down to 5 nm in size combined with the presence of amorphous materials and a crystallographic preferred orientation (CPO) (Table 2), remains intriguing.

Focusing on simulated calcite faults (Figures 4–6), the internal polycrystalline substructure observed in PSZs nanograins formed in LVF [113,114,140] as well as HVF experiments [93] bears a striking similarity to microstructures found in shocked ductile metals [148,149]. As in metals, the high ductility of calcite [150,151] may therefore allow the observed ~5–20 nm substructure to form by progressive development of nano-cell walls from dense dislocation networks and tangles generated by low temperature crystal-plasticity (e.g., r(104) slip or e(108) twinning [152]). Following from this, we speculate that plastic deformation and/or fracturing and abrasion occurring at parent grain surfaces led to the detachment of ~100 nm sized nanocrystalline clusters or fragments from these micron-sized parent grains [148,149]. The nanograins produced in turn rounded, to form the rolling, grain-neighbor-swapping nanospherules comprising the porous nanogranular PSZ [140]. To further unravel the formation mechanism of nanocrystallites and nanospherules in calcite gouge is a challenging task which requires more elaborate experiments and micro-/nanostructural analyses.

Amorphous materials may form by melt quenching, mechanical deformation, chemical reactions or a coupling between the latter two. Here, we focus on those materials derived from sub-solidus derived processes. For a thought-provoking investigation into chemo-mechanical- vs. melt-derived amorphous solids the reader is referred to Pec et al. [127]. In general, solid-state amorphization is attributed to arise from (1) the introduction of externally-derived mechanical instabilities (e.g., dislocations), (2) externally-forced volume expansion at constant temperature or (3) thermal expansion during heating at constant pressure [65,153]. By contrast, mechano-chemical interactions may produce amorphous materials as a result of the reduction of chemical species. This is particularly relevant in carbonate fault rocks where decarbonation reactions release CO_2 that can subsequently be reduced to (amorphous) carbon phases. Several natural [154–156] and experimental [93,115,118,140] studies of carbonate fault rocks have reported the occurs of amorphous carbon, often intimately associated with nanogranular calcites. The exact chemical pathways for CO_2 reduction to amorphous carbon remain, however, debated [115,156,157]. Additionally, in natural systems fluids can facilitate the precipitation of amorphous solids [158], making it difficult to discriminate internally- from externally-controlled formation mechanisms. Sub-solidus-derived amorphous materials are also widely reported in silicate-dominated systems (Table 2). The detailed mechanism(s) of amorphization, and more generally the impact of differences in atomic order on mechanical properties [159], on fault rheology, remains subject of further study.

Aside from the formation of nanocrystallites and amorphization within a PSZ, this does not explain the development of an internal CPO. Pozzi et al. [123] suggested that grain-size insensitive (GSI) creep mechanisms (dislocation creep) may explain CPO formation in a PSZ composed of 200–300 nm-sized grains formed in calcite gouge sheared at v = 1.4 m/s, at σ_n = 25 MPa. However, in the case of CPO-bearing PSZs formed in LVF tests, the porous structure observed in the bulk PSZ (Figure 6) is suggestive of nanogranular flow, which is not known for generating, or retaining a pre-existing, CPO. One potential mechanism for CPO formation in (nano-)granular flow may be through oriented interface attachment (OA), which is widely reported as a mechanism by which nanocrystallites can rapidly coalesce to form single crystals in numerous nanomaterials [160–162], including in calcite [163]. The thermodynamic driving force for particle coalescence in an OA event originates from crystallographic orientation-dependent, interatomic Coulombic interactions arising from both the surface atoms, and of atoms within the interior of the approaching nanoparticles [164,165]. Particle coalescence leads to a reduction of total surface energy [120], which, in the case of calcite would lead to an alignment of the lowest energy (104) plane [166], consistent with observations of simulated calcite faults deformed in LVF tests [113,114,140].

5.2. MSS-Bearing PSZs as Indicators for Past Seismic Slip?

Microstructural studies of simulated dolomite and limestone faults sheared in HVF experiments suggest the following characteristics of "glossy", "shiny" or "mirror-like" slip surfaces:

(i) They form only at high mechanical work input rates or power densities ($\dot{W} = \mu \cdot \sigma_n^{eff} \cdot v$, where μ is the coefficient of fault friction) [135,138].

(ii) They are at least in part responsible for the strong dynamic weakening often seen in samples sheared at co-seismic slip rates [137].

(iii) They are associated with dynamic recrystallization caused by heating at co-seismic slip rates [167].

However, the mirror-like surface patches formed in LVF experiments show very similar striated form and nanoscale topography [114,140] to those formed in HVF experiments, suggesting at least some degree of shared origin regardless of the areal extent or of shearing velocity. Moreover, a continuous MSS marking the PSZ has also been observed in simulated calcite gouge sheared at $0.1 \leq v \leq 100$ μms^{-1} (Figure 5c), which showed steady-state μ-values of ~0.5–0.6 (see [122,168] for data from experiments conducted under similar T-σ_n^{eff}-v conditions). These observations strongly suggest that MSSs are not related to any dynamic weakening mechanisms, and that their seismic origin remains debatable at

best. Rather, as pointed out by Pozzi et al. [139], MSSs seem to demarcate a rheological discontinuity between an ultrafine-grained zone, which internally deforms via thermally-activated and grain-size dependent deformation mechanisms, i.e., the PSZ, and the adjacent, coarser-grained wall rock, which deforms by brittle processes (grain fracturing). The fact that patchy MSSs formed in LVF tests are found at different topographic levels throughout the PSZ (Figure 6a) indicate that they probably formed as isolated patches rather than as a single, through-going film. Furthermore, at some locations within the broader nanogranular PSZ volume, nanofibers are observed outside MSSs, or bridging between the MSS and the porous PSZ (Figure 6b,c). Combining these observations, we hypothesize that, with further increasing displacement, nanofibers within the bulk PSZ will ultimately align to form a single through-going MSS.

From rotary shear experiments on cylindrical cores of dolomite and limestone performed at v = 0.002–0.96 m/s and ${\sigma_n}^{eff}$ = 0.25–6.9 MPa, Boneh et al. [138] showed that shiny striated slip-surface patches started to develop only at $\dot{W}$-values in excess of 30 kW/m^2. The cumulative area covered by these patches increased with increasing $\dot{W}$, ultimately producing a continuous, highly-reflective principal slip surface. Using experiments on simulated gouge prepared from dolostone, performed at v = 0.001–1.13 m/s and ${\sigma_n}^{eff}$ = 13–26 MPa, Fondriest et al. [135] showed that shiny surfaces only developed at $\dot{W}$ values > 40 kW/m^2, covering an area of the sample that progressively increases with increasing displacement. By contrast, the shiny patches developed in simulated calcite gouge reported in LVF tests (Figure 6) [114,140] formed at $\dot{W} = \mu \cdot \sigma_n^{eff} \cdot v$ = 50 MPa × (0.7 ± 0.1) × 10^{-6} m/s = 35 ± 5 W/m^2, i.e., 2 to 5 orders of magnitude lower than considered necessary for them to form in HVF experiments. This demonstrates that such shiny striates surfaces do not exclusively form at the high-power densities (>30–40 kW/m^2) associated with HVF experiments and with co-seismic slip rates. The implication is that mirror-like PSZs cannot be used as field indicators of past co-seismic slip in carbonates rocks without additional geological or microstructural evidence. The role of normal stress and cumulative displacement achieved in controlling the continuity of MSSs should be investigated further.

The development of highly-reflective PSZs in HVF experiments performed by Smith et al. [167], using simulated calcite gouge (v > 0.1 m/s, ${\sigma_n}^{eff}$ = 2–26 MPa, $\sum x$ > 1 m) was shown to be associated with the presence of dynamically recrystallized grains characterized by a CPO, adjacent to the slipping zone, while the PSZ itself was composed of statically recrystallized grains. Dynamic recrystallization here refers to the growth of internal strain- or defect-free grains during shear, whereas static recrystallization refers to such growth upon piston arrest and cooling after the experiment. In the experiments by Smith et al. [167], recrystallization and CPO formation were attributed to the attainment of high temperatures (650–900 °C) reflecting heat dissipated from the PSZ during localized frictional slip at co-seismic rates [167,169]. Static recrystallization of PSZ grains was inferred to have played a role in experiments performed by Verberne et al. [122], on simulated calcite gouge sheared at v = 100 µm/s (T = 550 °C, ${\sigma_n}^{eff}$ = 50 MPa, $\sum x$ = 10.4 mm) (Figure 5d). Grain growth upon cooling after the experiment suggests that the grain size within the PSZ may have been smaller during shear. MSS-bearing PSZs developed in LVF tests ($v < 10^{-4}$ ms^{-1}) using calcite gouge showed no evidence for conventional dynamic or static recrystallization, either in or adjacent to the PSZ, nor is this likely to have occurred considering the low slip rates, temperatures, and $\dot{W}$-values applying to these tests. The implication is that the presence of a statically recrystallized PSZ, with adjacent dynamically recrystallized grains, may indeed offer a useful constraint to past high-velocity slip, at least in limestones [167,170].

5.3. The Role of Nanocrystalline PSZs in Controlling Fault Stability

As mentioned in Section 2 above, in the case of earthquakes, fault sliding is believed to occur by stick-slip motion [38], caused by potentially unstable "velocity(v)-weakening" properties of the fault sliding medium [39–41,43]. The physical processes responsible for v-weakening behavior of gouge-filled faults are only recently beginning to be elucidated. Based on observations from fault analogue experiments using powdered halite-muscovite mixtures, Niemeijer & Spiers [33,171] developed a micromechanical model for shear deformation of granular fault rock. They showed that

competition between dilatant granular flow and compaction by water-assisted diffusive mass transfer leads to an increase in steady-state porosity with increasing shear rate, and v-weakening behavior [171]. However, any time-sensitive, Arrhenius-type deformation mechanism will, when in competition with time-insensitive dilatation or granular flow, produce v-weakening. This mechanism of competitive dilatation and compaction may well explain thermally-activated transitions in the v-dependence of friction seen in a wide range of fault rock types [168,172–174]. The extended "Chen-Niemeijer-Spiers" (CNS) model developed recently [175] is capable of quantitatively reproducing a wide range of laboratory fault gouge friction data using physically-based input parameters [176,177], therewith providing a powerful tool for numerical earthquake-cycle simulators [178].

To produce v-weakening in the CNS model, the rate of intergranular compaction ($\dot{\varepsilon}_{cp}$) and dilatation by granular flow ($\dot{\varepsilon}_{gr}$) within the deforming gouge zone must be within the same order of magnitude, i.e., $|\dot{\varepsilon}_{gr}| \approx |\dot{\varepsilon}_{cp}|$. Under conditions where either process dominates stable v-strengthening occurs. In the case of intergranular creep by water-assisted diffusive mass transfer, relevant for compaction of microgranular calcite up to 150 °C [179], the compactive strain rate $\dot{\varepsilon}_{cp}$ is described using [72]

$$\dot{\varepsilon}_{cp} = A \cdot \frac{\sigma \Omega}{RTd^3} \cdot DCS \cdot f(\varphi) \quad (1)$$

where A is a constant, σ is the (effective) axial stress, Ω is the molecular volume of the solid, D is the diffusion coefficient, C is the solubility of the solute, d is grain size, and $f(\varphi)$ is a porosity function (Table 3). In view of the inverse cubic dependence on d Equation (1), in the case of <100 nm sized particles in nanocrystalline PSZs, compaction by water-assisted diffusive mass transfer is expected to be very fast, even at relatively low temperatures.

Table 3. Values/expressions used for the terms appearing in Equation (1).

Term	Formula/Value	Source
A	$576/3\pi \approx 61$	Pluymakers & Spiers [180]
σ	50×10^6 Pa	Verberne et al. [140]
d	1×10^{-7} m	Figure 6
T	291 to 423 K	Verberne et al. [140]
Ω	3.69×10^{-5} m^3 mol^{-1}	Zhang et al. [179]
$f(\phi)$	$f(\phi) \approx 2\phi/(1-2\phi)^2 \approx 1.1$	Pluymakers & Spiers [180]
Water-assisted diffusive mass transfer:		
D	$D = D_0 \exp\left(-\frac{Q}{RT}\right)$ $D = 1 \times 10^{-10}$ m^2·s^{-1} at T = 298 K $Q = 1.5 \times 10^4$ J·mol^{-1}	Nakashima [181]
C	$C = \sqrt{K_s}$ $\log K_s = -171.9605 - 0.077993T + \frac{2839.319}{T} + \log T$	Plummer & Busenberg [182]
S	1 to 2×10^{-9} m	Verberne et al. [140]
Solid-state grain boundary diffusion:		
DS	$DS = (DS)_0 \exp\left(-\frac{Q_d}{RT}\right)$ $(DS)_0 = 1.5 \times 10^{-9}$ m^3·s^{-1} $Q_d = 2.67 \times 10^5$ J·mol^{-1}	Farver & Yund [183]

In the case of solid-state grain boundary diffusion C = 1.

In Figure 7 we plot Equation (1) for the case of granular calcite, assuming grain sizes in the range from 5 nm to 1 µm. We also indicate the conditions of temperature (25–150 °C) and intergranular dilatation rate ($|\dot{\varepsilon}_{gr}| \approx 10^{-2}10^{0}$ s^{-1}) characterizing the PSZ developed in LVF experiments on simulated calcite faults (Figure 4a,b and Figure 6) [140]. This shows that for 100 to 500 nm-sized grains $|\dot{\varepsilon}_{gr}| \approx |\dot{\varepsilon}_{cp}|$ (Figure 7a), implying that under the conditions of normal stress and temperature used here (Table 3) v-weakening may be observed. Combined with the ~100 nm-sized nanospherules and -fibers observed in the broader

PSZ (Figure 6), this suggest that the mechanism of competitive dilation and compaction [33,171] can explain the thermally-activated transition from stable v-strengthening to unstable v-weakening seen at ~100 °C in experiments on simulated calcite(-rich) fault gouge [114,124,168,184,185]. For grains <100 nm size, this mechanism is not expected to be relevant when assuming intergranular creep by water-assisted diffusive mass transfer. However, equation 1 can also be used to assess creep rates assuming solid-state diffusion involving mass transfer through a grain boundary of thickness S [70]. This shows that for grain sizes down to 10 nm, $\dot{\varepsilon}_{cp} \approx 10^{-3}$ s^{-1} at temperatures > 650 °C (Figure 7b). Such high temperatures are common in HVF experiments, suggesting that the mechanism of competitive compaction and dilation may also play a role at co-seismic slip rates. This is consistent with claims that superplastic deformation of nanogranular fault rock controls (dynamic) fault rupture [93,116,186].

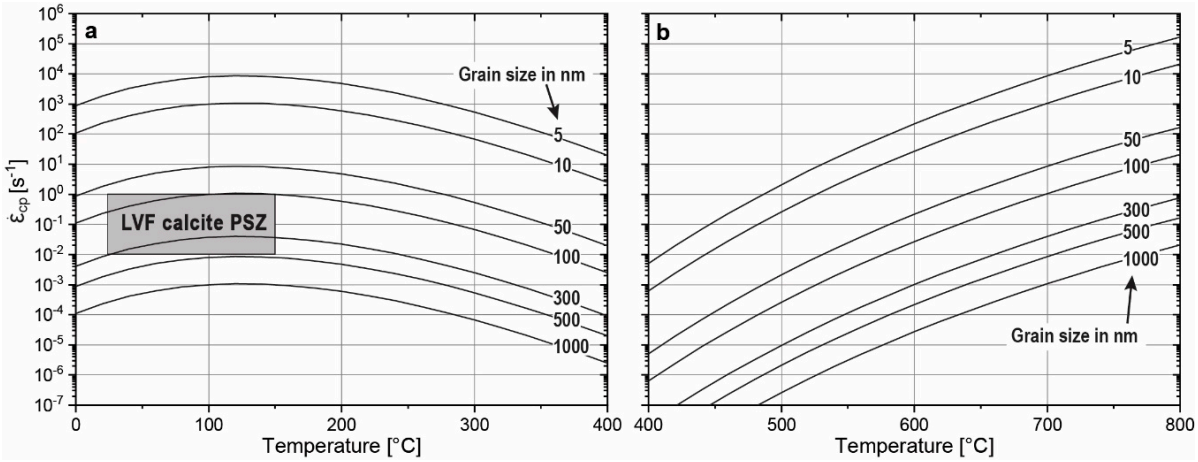

Figure 7. Intergranular compaction creep strain rates in granular calcite versus temperature for grain size d. (**a**). Water-assisted diffusive mass transfer. The grey shaded area indicates the conditions characterizing the PSZ developed in LVF experiments using simulated calcite gouge (Figure 4a,b and Figure 6) [140] (**b**). Solid-state grain boundary diffusion. For a list of parameters used see Table 3.

Notwithstanding all of the above, the micromechanical framework underlying the CNS model [171,175] is of course highly idealized. The model assumptions are reasonable at low slip rates, but break down when frictional heating and associated dynamic fault rupture processes come into play [57,61,62]. Another potentially problematical aspect is the knowledge and quantification of the relevant intergranular creep mechanisms. In view of the unusual deformation properties of nanocrystalline materials (Figure 2), extrapolation of data from compaction experiments using microcrystalline samples to the nanometer realm may be unreasonable. Parameter values and expressions such as listed in Table 3 have to be re-assessed in the case of nanocrystalline fault rock.

5.4. Implications for Natural Faulting in the Seismogenic Zone

In the above we have shown that the Chen-Niemeijer-Spiers (CNS) model describing competitive dilatant nanogranular flow and nanospherule/-fiber compaction may explain the transition from stable velocity strengthening to potentially unstable velocity weakening at temperatures ~80–100 °C seen in calcite fault rock [114,124,168,184,185]. This transition is consistent with the location of the upper seismogenic limit at shallow depths (~2–4 km) in tectonically-active limestone terrains, such as those characterizing the Mediterranean region [187–189]. Velocity weakening hence seismogenic fault slip on nanogranular PSZs becomes possible because (water-assisted) diffusive mass transfer is dramatically accelerated by the nanogranular nature of the slip zone rock that forms. Given the abundant observations of nanogranular fault surfaces in fault rocks of all types (Tables 1 and 2), and the fast diffusion rates in nanostructured materials [11,69,75], the mechanism of dilatation versus

compaction, applied to sheared nanogranular fault rock, may be generally relevant in controlling the upper limit of the seismogenic zone.

In the CNS model framework, a comparison between fault rock creep rates and fault zone shear strain rates may yield clues on the depth to the limits seismogenic zone, i.e., taking the condition that $|\dot{\varepsilon}_{gr}| \approx |\dot{\varepsilon}_{cp}|$ may lead to unstable seismogenic fault-slip [33,140,171]. To illustrate this, we used Equation (1) for the case of calcite (Table 3) to plot grain size vs. depth curves for different $\dot{\varepsilon}_{cp}$, assuming a geothermal gradient of 30 °C/km and a density of 2700 kg/m^{-3} (Figure 8). Crustal fault zone shear strain rates remain poorly constrained, mainly because of the lack of observations on the width of the actively deforming zone [190]. Nonetheless, using the "commonly cited value" for upper-crustal fault zone shear strain rates of ~10^{-14} s^{-1} [190,191] for $\dot{\varepsilon}_{gr}$ in Equation (1) (Figure 8), shows that solid state creep may be relevant in grains <100 nm in size at ~3–4 km depth. This is close to the upper limit of the seismogenic zone in tectonically-active carbonate terrains [187–189]. However, importantly, in the above analysis using the compaction-dilation model, the processes controlling nanograin formation and the role of grain growth are ignored. Especially the latter potentially presents a major limitation, since at greater depths/temperatures static as well as dynamic recrystallization of PSZ grains are expected to play a role [147,192]. Future models aiming to describe the physical processes leading to dynamic fault rupture should take into account the progressive development of fault rocks with increasing shear strain, i.e., specifically, the competition between grain growth and grain size reduction the PSZ.

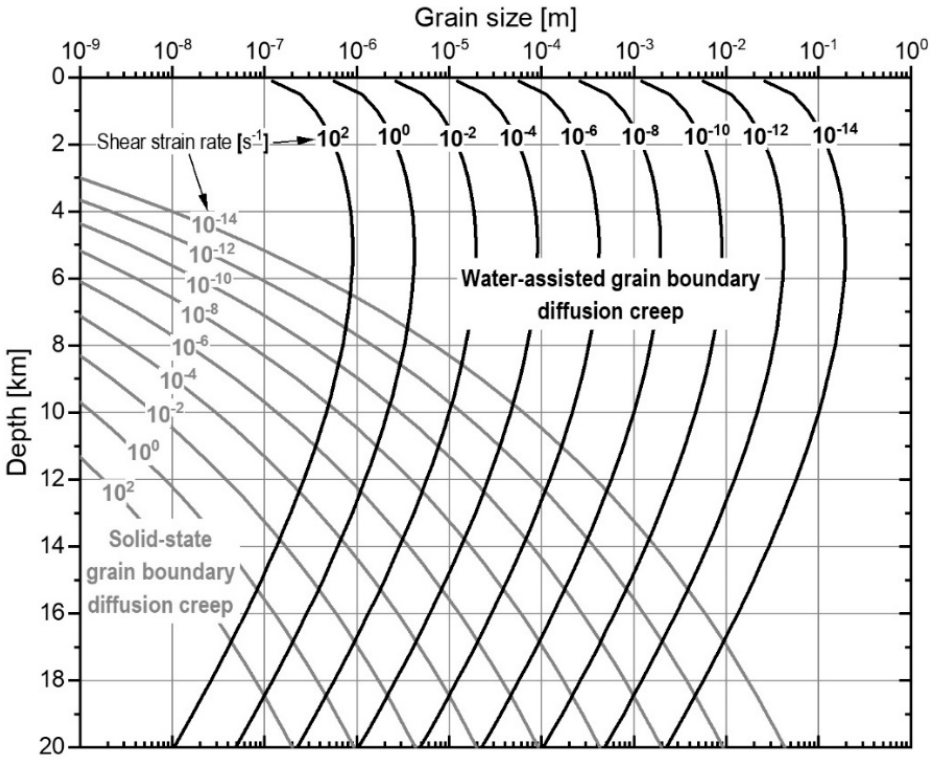

Figure 8. Water-assisted and solid-state grain boundary diffusion creep in calcite (Equation (1)), plotted as grain size vs. depth (taking 30 °C/km and a density of 2700 kg m^{-3}). For a list of parameters used see Table 3.

6. Conclusions

Nanocrystalline fault rock is consistently observed in natural and experimentally-formed principal slip zones (PSZs) and is frequently associated with the presence of a crystallographic preferred orientation (CPO), (partly) amorphized materials, and ultra-smooth interfaces known as "glossy", "shiny" or "mirror-like" slip surfaces (MSSs). Experiments conducted under a wide range of normal

stresses, temperatures, and displacement rates demonstrate that these features can be produced over a wide range of conditions pertaining to upper-crustal fault-slip, covering co-seismic and sub-seismic displacement rates. Simple calculations using constitutive equations for compaction by water-assisted diffusive mass transfer, combined with existing models for velocity-weakening shear of gouge-filled faults, show that nanogranular fault rock plays a key role in controlling the depth to the upper-limit of the seismogenic zone. In view of the unusual deformation properties of nanocrystalline (NC) materials, an important task in Earth sciences is to improve insights on the rheology of NC PSZs, or of nanophased geomaterials in general.

Supplementary Materials: The following are available online at http://www.mdpi.com/2075-163X/9/6/328/s1, Video S1: unif_biref-[CaCO3-RT-dry].

Author Contributions: Conceptualization, B.A.V. and O.P.; methodology, B.A.V.; software, N/A; validation, B.A.V., O.P. and C.J.S.; formal analysis, B.A.V.; investigation, B.A.V.; resources, C.J.S.; data curation, B.A.V.; writing—original draft preparation, B.A.V.; writing—review & editing B.A.V., O.P., C.J.S.; visualization, B.A.V., O.P.; supervision, C.J.S.; project administration, B.A.V.; funding acquisition, B.A.V., C.J.S.

Funding: Part of this work was conducted within the framework of B.A.V.'s Ph.D. thesis, which was supported by grant 2011-75 awarded by the Netherlands Centre for Integrated Solid Earth Science (ISES). B.A.V. is now supported by JSPS KAKENHI grant #19K14823.

Acknowledgments: The authors thank André Niemeijer, Hans de Bresser, Jianye Chen, Colin Peach, Virginia Toy, and Martyn Drury for discussions at various stages of this work. Matthijs de Winter is thanked for preparing the FIB-section in sample lmst@150 °C (Figure 4b). Michael Hochella, Li-Wei Kuo, and Hiroko Kitajima are thanked for helping with literature. We thank two anonymous reviewers for helpful input that improved the paper significantly.

Conflicts of Interest: The authors declare no conflicts of interest.

References

1. Banfield, J.F.; Zhang, H.-Z. Nanoparticles in the environment. *Rev. Mineral. Geochem.* **2001**, *44*, 1–58. [CrossRef]
2. Hochella, M.F., Jr. Nanoscience and technology the next revolution in the Earth sciences. *Earth Planet. Sci. Lett.* **2002**, *203*, 593–605. [CrossRef]
3. Hochella, M.F., Jr.; Lower, S.K.; Maurice, P.A.; Penn, R.L.; Sahai, N.; Sparks, D.L.; Twining, B.S. Nominerals, mineral nanoparticles, and Earth systems. *Science* **2008**, *319*, 1631–1635. [CrossRef] [PubMed]
4. Hochella, M.F., Jr.; Mogk, D.W.; Ranville, J.; Allen, I.C.; Luther, G.W.; Marr, L.C.; McGrail, B.P.; Muruyama, M.; Qafoku, N.P.; Rosso, K.M.; et al. Natural, incidental, and engineered nanomaterials and their impacts on the Earth system. *Science* **2019**, *363*, 10. [CrossRef] [PubMed]
5. Ju, Y.; Huang, C.; Sun, Y.; Wan, Q.; Lu, X.; Lu, S.; He, H.; Wang, X.; Zou, C.; Wu, J.; et al. Nanogeosciences: Research History, Current Status, and Development Trends. *J. Nanosci. Nanotechnol.* **2017**, *17*, 5930–5965. [CrossRef]
6. Wilson, B.; Dewers, T.; Reches, Z.; Brune, J. Particle size and energetics of gouge from earthquake rupture zones. *Nature* **2005**, *434*, 749–752. [CrossRef] [PubMed]
7. Chester, J.S.; Chester, F.M.; Kronenberg, A.K. Fracture surface energy of the Punchbowl fault, San Andreas system. *Nature* **2005**, *437*, 133–136. [CrossRef] [PubMed]
8. Ma, K.; Tanaka, H.; Song, S.; Wang, C.; Hung, J.; Tsai, Y.; Mori, J.; Song, Y.; Yeh, E.; Soh, W.; et al. Slip zone and energetics of a large earthquake from the Taiwan Chelungpu-fault Drilling Project. *Nature* **2006**, *444*, 473–476. [CrossRef]
9. Sibson, R.H. Earthquakes and rock deformation in crustal fault zones. *Annu. Rev. Earth Planet. Sci.* **1986**, *14*, 149–175. [CrossRef]
10. Sibson, R.H. Thickness of the seismic slip zone. *Bull. Seismol. Soc. Am.* **2003**, *93*, 1169–1178. [CrossRef]
11. Tjong, S.; Chen, H. Nanocrystalline materials and coatings. *Mater. Sci. Eng.* **2004**, *45*, 1–88. [CrossRef]
12. Meyers, M.; Mishra, A.; Benson, D. Mechanical properties of nanocrystalline materials. *Prog. Mater. Sci.* **2006**, *51*, 427–556. [CrossRef]
13. Rogers, B.; Adams, J.; Pennathur, S. *Nanotechnology: Understanding Small Systems*, 3rd ed.; CRC Press Taylor & Francis Group: Boca Raton, FL, USA, 2015; p. 407.

14. Rutter, E.; Holdsworth, R.; Knipe, R.; Strachan, R.; Magloughlin, J. The nature and tectonic significance of fault-zone weakening: An introduction. *Nat. Tecton. Signif. Fault Zone Weaken.* **2001**, *186*, 1–11. [CrossRef]
15. Holdsworth, R.E.; Stewart, M.; Imber, J.; Strachan, R.A. The strucure and rheological evolution of reactivated continental fault zones: A review and case study. In *Continental Reactivation and Reworking*; Miller, J., Holdsworth, R.E., Buick, I.S., Hand, M., Eds.; Geological Society: London, UK, 2001; Volume 184, pp. 115–137.
16. Brace, W.F.; Kohlstedt, D.L. Limits on lithospheric stress imposed by laboratory experiments. *J. Geophys. Res.* **1980**, *85*, 6248–6252. [CrossRef]
17. Kohlstedt, D.L.; Evans, B.; Mackwell, S.J. Strength of the lithosphere—Constraints imposed by laboratory experiments. *J. Geophys. Res. Solid Earth* **1995**, *100*, 17587–17602. [CrossRef]
18. Sibson, R.H. Fault zone models, heat-flow, and the depth distribution of earthquakes in the continental crust of the united states. *Bull. Seismol. Soc. Am.* **1982**, *72*, 151–163.
19. Sibson, R.H. Continental fault structure and the shallow earthquake source. *J. Geol. Soc.* **1983**, *140*, 741–767. [CrossRef]
20. Sibson, R.H. Roughness at the base of the seismogenic zone—Contributing factors. *J. Geophys. Res.* **1984**, *89*, 5791–5799. [CrossRef]
21. Meissner, R.; Strehlau, J. Limits of stresses in continental crusts and their relation to the depth-frequency distribution of shallow earthquakes. *Tectonics* **1982**, *1*, 73–89. [CrossRef]
22. Scholz, C.H. The brittle-plastic transition and the depth of seismic faulting. *Geol. Rundsch.* **1988**, *77*, 319–328. [CrossRef]
23. Shimamoto, T. The origin of S-C mylonites and a new fault-zone model. *J. Struct. Geol.* **1989**, *11*, 51–64. [CrossRef]
24. Scholz, C.H. *The Mechanics of Earthquakes and Faulting*, 2nd ed.; Cambridge University Press: Cambridge, UK, 2002; p. 471.
25. Fagereng, Å.; Toy, V.G.; Rowland, J.V. Geology of the earthquake source: An introduction. *Geol. Earthq. Sour.* **2011**, *359*, 1–16. [CrossRef]
26. Marone, C.; Scholz, C.H. The depth of seismic faulting and the upper transition from stable to unstable regimes. *Geophys. Res. Lett.* **1988**, *15*, 621–624. [CrossRef]
27. Chester, F.M.; Higgs, N.G. Multimechanism friction constitutive model for ultrafine quartz gouge at hypocentral conditions. *J. Geophys. Res.-Solid Earth* **1992**, *97*, 1859–1870. [CrossRef]
28. Reinen, L.A.; Tullis, T.E.; Weeks, J.D. Two-mechanism model for frictional sliding of serpentinite. *Geophys. Res. Lett.* **1992**, *19*, 1535–1538. [CrossRef]
29. Chester, F.M. Effects of temperature on friction—Constitutive equations and experiments with quartz gouge. *J. Geophys. Res.-Solid Earth* **1994**, *99*, 7247–7261. [CrossRef]
30. Stewart, M.; Holdsworth, R.; Strachan, R. Deformation processes and weakening mechanisms within the frictional-viscous transition zone of major crustal-scale faults: Insights from the Great Glen Fault Zone, Scotland. *J. Struct. Geol.* **2000**, *22*, 543–560. [CrossRef]
31. Bos, B.; Spiers, C. Fluid-assisted healing processes in gouge-bearing faults: Insights from experiments on a rock analogue system. *Pure Appl. Geophys.* **2002**, *159*, 2537–2566. [CrossRef]
32. Bos, B.; Spiers, C. Frictional-viscous flow of phyllosilicate-bearing fault rock: Microphysical model and implications for crustal strength profiles. *J. Geophys. Res.-Solid Earth* **2002**, *107*. [CrossRef]
33. Niemeijer, A.; Spiers, C. Velocity dependence of strength and healing behaviour in simulated phyllosilicate-bearing fault gouge. *Tectonophysics* **2006**, *427*, 231–253. [CrossRef]
34. Imber, J.; Holdsworth, R.E.; Smith, S.A.F.; Jefferies, S.P.; Collettini, C. Frictional-viscous flow, seismicity and the geology of weak faults: A review and future directions. In *Internal Structure of Fault Zones: Implications for Mechanical and Fluid-Flow Properties*; Wibberley, C.A.J., Kurz, W., Imber, J., Holdsworth, R.E., Collettini, C., Eds.; Geological Society: London, UK, 2008; Volume 299, pp. 151–173.
35. Noda, H.; Shimamoto, T. A rate- and state-dependent ductile flow law of polycrystalline halite under large shear strain and implications for transition to brittle deformation. *Geophys. Res. Lett.* **2010**, *37*. [CrossRef]
36. Noda, H.; Shimamoto, T. Transient behavior and stability analyses of halite shear zones with an empirical rate-and-state friction to flow law. *J. Struct. Geol.* **2012**, *38*, 234–242. [CrossRef]
37. Nicolas, A.; Fortin, J.; Regnet, J.B.; Verberne, B.A.; Plumper, O.; Dimanov, A.; Spiers, C.J.; Gueguen, Y. Brittle and semibrittle creep of Tavel limestone deformed at room temperature. *J. Geophys. Res. Solid Earth* **2017**, *122*, 4436–4459. [CrossRef]

38. Brace, W.F.; Byerlee, J.D. Stick-slip as a mechanism for earthquakes. *Science* **1966**, *153*, 990–992. [CrossRef] [PubMed]
39. Dieterich, J.H. Time-dependent friction and mechanics of stick-slip. *Pure Appl. Geophys.* **1978**, *116*, 790–806. [CrossRef]
40. Dieterich, J.H. Modeling of rock friction 1. Experimental results and constitutive equations. *J. Geophys. Res.* **1979**, *84*, 2161–2168. [CrossRef]
41. Ruina, A.L. Slip stability and state variable friction laws. *J. Geophys. Res.* **1983**, *88*, 359–370. [CrossRef]
42. Baumberger, T.; Heslot, F.; Perrin, B. Crossover from creep to inertial motion in friction dynamics. *Nature* **1994**, *367*, 544–546. [CrossRef]
43. Rice, J.R.; Ruina, A.L. Stability of steady frictional slipping. *J. Appl. Mech.* **1983**, *50*, 343–349. [CrossRef]
44. Scholz, C.H. Earthquakes and friction laws. *Nature* **1998**, *391*, 37–42. [CrossRef]
45. Sibson, R.H. Fault rocks and fault mechanisms. *J. Geol. Soc.* **1977**, *133*, 191–213. [CrossRef]
46. Chester, F.M.; Chester, J.S. Ultracataclasite structure and friction processes of the Punchbowl fault, San Andreas system, California. *Tectonophysics* **1998**, *295*, 199–221. [CrossRef]
47. Mitchell, T.; Faulkner, D. The nature and origin of off-fault damage surrounding strike-slip fault zones with a wide range of displacements: A field study from the Atacama fault system, northern Chile. *J. Struct. Geol.* **2009**, *31*, 802–816. [CrossRef]
48. Smith, S.A.F.; Billi, A.; Di Toro, G.; Spiess, R. Principal Slip Zones in Limestone: Microstructural Characterization and Implications for the Seismic Cycle (Tre Monti Fault, Central Apennines, Italy). *Pure Appl. Geophys.* **2011**, *168*, 2365–2393. [CrossRef]
49. Barth, N.; Boulton, C.; Carpenter, B.; Batt, G.; Toy, V. Slip localization on the southern Alpine Fault, New Zealand. *Tectonics* **2013**, *32*, 620–640. [CrossRef]
50. Li, H.; Wang, H.; Xu, Z.; Si, J.; Pei, J.; Li, T.; Huang, Y.; Song, S.; Kuo, L.; Sun, Z.; et al. Characteristics of the fault-related rocks, fault zones and the principal slip zone in the Wenchuan Earthquake Fault Scientific Drilling Project Hole-1 (WFSD-1). *Tectonophysics* **2013**, *584*, 23–42. [CrossRef]
51. Kuo, L.; Hsiao, H.; Song, S.; Sheu, H.; Suppe, J. Coseismic thickness of principal slip zone from the Taiwan Chelungpu fault Drilling Project-A (TCDP-A) and correlated fracture energy. *Tectonophysics* **2014**, *619*, 29–35. [CrossRef]
52. Shigematsu, N.; Kametaka, M.; Inada, N.; Miyawaki, M.; Miyakawa, A.; Kameda, J.; Togo, T.; Fujimoto, K. Evolution of the Median Tectonic Line fault zone, SW Japan, during exhumation. *Tectonophysics* **2017**, *696*, 52–69. [CrossRef]
53. Shipton, Z.; Evans, J.; Abercrombie, R.; Brodsky, E.; Abercrombie, R.; McGarr, A.; DiToro, G.; Kanamori, H. The missing sinks: Slip localization in faults, damage zones, and the seismic energy budget. *Earthq. Radiat. Energy Phys. Fault.* **2006**, *170*, 217. [CrossRef]
54. Lockner, D.A.; Byerlee, J.D.; Kuksenko, V.; Ponomarev, A.; Sidorin, A. Quasi-static fault growth and shear fracture energy in granite. *Nature* **1991**, *350*, 39–42. [CrossRef]
55. Marone, C. Laboratory-derived friction laws and their application to seismic faulting. *Annu. Rev. Earth Planet. Sci.* **1998**, *26*, 643–696. [CrossRef]
56. Ikari, M.J. Principal slip zones: Precursors but not recorders of earthquake slip. *Geology* **2015**, *43*, 955–958. [CrossRef]
57. Rice, J. Heating and weakening of faults during earthquake slip. *J. Geophys. Res. Solid Earth* **2006**, *111*. [CrossRef]
58. Han, R.; Shimamoto, T.; Hirose, T.; Ree, J.; Ando, J. Ultralow friction of carbonate faults caused by thermal decomposition. *Science* **2007**, *316*, 878–881. [CrossRef] [PubMed]
59. De Paola, N.; Hirose, T.; Mitchell, T.; Di Toro, G.; Viti, C.; Shimamoto, T. Fault lubrication and earthquake propagation in thermally unstable rocks. *Geology* **2011**, *39*, 35–38. [CrossRef]
60. Di Toro, G.; Hirose, T.; Nielsen, S.; Pennacchioni, G.; Shimamoto, T. Natural and experimental evidence of melt lubrication of faults during earthquakes. *Science* **2006**, *311*, 647–649. [CrossRef] [PubMed]
61. Di Toro, G.; Han, R.; Hirose, T.; De Paola, N.; Nielsen, S.; Mizoguchi, K.; Ferri, F.; Cocco, M.; Shimamoto, T. Fault lubrication during earthquakes. *Nature* **2011**, *471*, 494–498. [CrossRef]
62. Platt, J.; Brantut, N.; Rice, J. Strain localization driven by thermal decomposition during seismic shear. *J. Geophys. Res. Solid Earth* **2015**, *120*, 4405–4433. [CrossRef]

63. Chen, J.; Niemeijer, A.; Fokker, P. Vaporization of fault water during seismic slip. *J. Geophys. Res. Solid Earth* **2017**, *122*, 4237–4276. [CrossRef]
64. Couchman, P.R.; Jesser, W.A. Thermodynamic theory of size dependence of melting temperature in metals. *Nature* **1977**, *269*, 481–483. [CrossRef]
65. Fecht, H.J. Defect-induced melting and solid-state amorphization. *Nature* **1992**, *356*, 133–135. [CrossRef]
66. Qi, W.; Wang, M. Size effect on the cohesive energy of nanoparticle. *J. Mater. Sci. Lett.* **2002**, *21*, 1743–1745. [CrossRef]
67. Buffat, P.; Borel, J.P. Size effect on melting temperature of gold particles. *Phys. Rev. A* **1976**, *13*, 2287–2298. [CrossRef]
68. Wang, S.; Cui, Z.; Xia, X.; Xue, Y. Size-dependent decomposition temperature of nanoparticles: A theoretical and experimental study. *Physica B* **2014**, *454*, 175–178. [CrossRef]
69. Wurschum, R.; Herth, S.; Brossmann, U. Diffusion in nanocrystalline metals and alloys—A status report. *Adv. Eng. Mater.* **2003**, *5*, 365–372. [CrossRef]
70. Coble, R.L. A model for boundary diffusion controlled creep in polycrystalline materials. *J. Appl. Phys.* **1963**, *34*, 1679–1682. [CrossRef]
71. Ashby, M.F.; Verrall, R.A. Diffusion-accommodated flow and superplasticity. *Acta Metall. Mater.* **1973**, *21*, 149–163. [CrossRef]
72. Rutter, E.H. Kinetics of rock deformation by pressure solution. *Philos. Trans. R. Soc. A* **1976**, *283*, 203–219. [CrossRef]
73. Lu, L.; Sui, M.; Lu, K. Superplastic extensibility of nanocrystalline copper at room temperature. *Science* **2000**, *287*, 1463–1466. [CrossRef]
74. Mohamed, F.; Li, Y. Creep and superplasticity in nanocrystalline materials: Current understanding and future prospects. *Mater. Sci. Eng. A Struct.* **2001**, *298*, 1–15. [CrossRef]
75. Mohamed, F. Deformation mechanism maps for micro-grained, ultrafine-grained, and nano-grained materials. *Mater. Sci. Eng. A Struct.* **2011**, *528*, 1431–1435. [CrossRef]
76. Hall, E.O. The deformation and ageing of mild steel 3. Discussion of results. *Proc. Phys. Soc. Lond. B* **1951**, *64*, 747–753. [CrossRef]
77. Petch, N.J. The cleavage strength of polycrystals. *J. Iron Steel Inst.* **1953**, *174*, 25–28.
78. Louchet, F.; Weiss, J.; Richeton, T. Hall-Petch law revisited in terms of collective dislocation dynamics. *Phys. Rev. Lett.* **2006**, *97*. [CrossRef] [PubMed]
79. Carlton, C.E.; Ferreira, P.J. What is behind the inverse Hall-Petch effect in nanocrystalline materials? *Acta Mater.* **2007**, *55*, 3749–3756. [CrossRef]
80. Ma, E. Watching the nanograins roll. *Science* **2004**, *305*, 623–624. [CrossRef]
81. Shan, Z.; Stach, E.; Wiezorek, J.; Knapp, J.; Follstaedt, D.; Mao, S. Grain boundary-mediated plasticity in nanocrystalline nickel. *Science* **2004**, *305*, 654–657. [CrossRef]
82. Carlton, C.E.; Ferreira, P.J. Dislocation motion-induced strain in nanocrystalline materials: Overlooked considerations. *Mater. Sci. Eng. A Struct.* **2008**, *486*, 672–674. [CrossRef]
83. Power, W.L.; Tullis, T.E. The relationship between slickenside surfaces in fine-grained quartz and the seismic cycle. *J. Struct. Geol.* **1989**, *11*, 879–893. [CrossRef]
84. Chester, J.S.; Goldsby, D.L. *Microscale Characterization of Natural and Experimental Slip Surfaces Relevant to Earthquake Mechanics*; South California Earthquake Center: Los Angeles, CA, USA, 2003.
85. Kuo, L.; Song, S.; Suppe, J.; Yeh, E. Fault mirrors in seismically active fault zones: A fossil of small earthquakes at shallow depths. *Geophys. Res. Lett.* **2016**, *43*, 1950–1959. [CrossRef]
86. Janssen, C.; Wirth, R.; Rybacki, E.; Naumann, R.; Kemnitz, H.; Wenk, H.; Dresen, G. Amorphous material in SAFOD core samples (San Andreas Fault): Evidence for crush-origin pseudotachylytes? *Geophys. Res. Lett.* **2010**, *37*. [CrossRef]
87. Siman-Tov, S.; Aharonov, E.; Sagy, A.; Emmanuel, S. Nanograins form carbonate fault mirrors. *Geology* **2013**, *41*, 703–706. [CrossRef]
88. Kirkpatrick, J.; Rowe, C.; White, J.; Brodsky, E. Silica gel formation during fault slip: Evidence from the rock record. *Geology* **2013**, *41*, 1015–1018. [CrossRef]
89. Evans, J.; Prante, M.; Janecke, S.; Ault, A.; Newell, D. Hot faults: Iridescent slip surfaces with metallic luster document high-temperature ancient seismicity in the Wasatch fault zone, Utah, USA. *Geology* **2014**, *42*, 623–626. [CrossRef]

90. Viti, C.; Brogi, A.; Liotta, D.; Mugnaioli, E.; Spiess, R.; Dini, A.; Zucchi, M.; Vannuccini, G. Seismic slip recorded in tourmaline fault mirrors from Elba Island (Italy). *J. Struct. Geol.* **2016**, *86*, 1–12. [CrossRef]
91. Beckmann, P.; Spizzichino, A. *The Scattering of Electromagnetic Waves from Rough Surfaces*; Pergamon Press: Oxford, UK, 1963; Volume 4.
92. Ozawa, K.; Takizawa, S. Amorphous material formed by the mechanochemical effect in natural pseudotachylyte of crushing origin: A case study of the Iida-Matsukawa Fault, Nagano Prefecture, Central Japan. *J. Struct. Geol.* **2007**, *29*, 1855–1869. [CrossRef]
93. De Paola, N.; Holdsworth, R.; Viti, C.; Collettini, C.; Bullock, R. Can grain size sensitive flow lubricate faults during the initial stages of earthquake propagation? *Earth Planet. Sci. Lett.* **2015**, *431*, 48–58. [CrossRef]
94. Viti, C. Exploring fault rocks at the nanoscale. *J. Struct. Geol.* **2011**, *33*, 1715–1727. [CrossRef]
95. Sibson, R.H. Generation of pseudotachylyte by ancient seismic faulting. *Geophys. J. Int.* **1975**, *43*, 775–794. [CrossRef]
96. Spray, J.G. Pseudotachylyte controversy—Fact or friction? *Geology* **1995**, *23*, 1119–1122. [CrossRef]
97. Cowan, D. Do faults preserve a record of seismic slip? A field geologist's opinion. *J. Struct. Geol.* **1999**, *21*, 995–1001. [CrossRef]
98. Rowe, C.; Griffith, W. Do faults preserve a record of seismic slip: A second opinion. *J. Struct. Geol.* **2015**, *78*, 1–26. [CrossRef]
99. Wenk, H.R. Are pseudotachylytes products of fracture or fusion? *Geology* **1978**, *6*, 507–511. [CrossRef]
100. Keulen, N.; Heilbronner, R.; Stünitz, H.; Boullier, A.; Ito, H. Grain size distributions of fault rocks: A comparison between experimentally and naturally deformed granitoids. *J. Struct. Geol.* **2007**, *29*, 1282–1300. [CrossRef]
101. Bullock, R.; De Paola, N.; Holdsworth, R.; Trabucho-Alexandre, J. Lithological controls on the deformation mechanisms operating within carbonate-hosted faults during the seismic cycle. *J. Struct. Geol.* **2014**, *58*, 22–42. [CrossRef]
102. Collettini, C.; Carpenter, B.; Viti, C.; Cruciani, F.; Mollo, S.; Tesei, T.; Trippetta, F.; Valoroso, L.; Chiaraluce, L. Fault structure and slip localization in carbonate-bearing normal faults: An example from the Northern Apennines of Italy. *J. Struct. Geol.* **2014**, *67*, 154–166. [CrossRef]
103. Demurtas, M.; Fondriest, M.; Balsamo, F.; Clemenzi, L.; Storti, F.; Bistacchi, A.; Di Toro, G. Structure of a normal seismogenic fault zone in carbonates: The Vado di Como Fault, Campo Imperatore, Central Apennines (Italy). *J. Struct. Geol.* **2016**, *90*, 185–206. [CrossRef]
104. Siman-Tov, S.; Stock, G.; Brodsky, E.; White, J. The coating layer of glacial polish. *Geology* **2017**, *45*, 987–990. [CrossRef]
105. Smeraglia, L.; Billi, A.; Carminati, E.; Cavallo, A.; Doglioni, C. Field- to nano-scale evidence for weakening mechanisms along the fault of the 2016 Amatrice and Norcia earthquakes, Italy. *Tectonophysics* **2017**, *712*, 156–169. [CrossRef]
106. Tullis, T.E.; Tullis, J. Experimental rock deformation techniques. In *Mineral and Rock Deformation: Laboratory Studies*, 36th ed.; Hobbs, B.E., Heard, H.C., Eds.; AGU: Washington, DC, USA, 1986; pp. 297–324.
107. Niemeijer, A.; Di Toro, G.; Griffith, W.; Bistacchi, A.; Smith, S.; Nielsen, S. Inferring earthquake physics and chemistry using an integrated field and laboratory approach. *J. Struct. Geol.* **2012**, *39*, 2–36. [CrossRef]
108. Ma, S.; Shimamoto, T.; Lu, Y.; Togo, T.; Kitajima, H. A rotary-shear low to high-velocity friction apparatus in Beijing to study rock friction at plate to seismic slip rates. *Earthq. Sci.* **2014**, *27*, 469–497. [CrossRef]
109. Logan, J.M.; Friedman, M.; Higgs, N.; Dengo, C.A.; Shimamoto, T. Experimental studies of simulated gouge and their application to studies of natural fault zones. In Proceedings of the Conference VIII—Analysis of Actual Fault Zones in Bedrock, Menlo Park, CA, USA, 1–5 April 1979; pp. 305–343.
110. Logan, J.M.; Dengo, C.A.; Higgs, N.G.; Wang, Z.Z. Fabrics of experimental fault zones: Their development and relationship to mechanical behavior. In *Fault Mechanics and TRANSPORT Properties in Rocks*; Evans, B., Wong, T.-F., Eds.; Academic Press: London, UK, 1992; pp. 33–68.
111. Yund, R.A.; Blanpied, M.L.; Tullis, T.E.; Weeks, J.D. Amorphous material in high-strain experimental fault gouges. *J. Geophys. Res.* **1990**, *95*, 15589–15602. [CrossRef]
112. Han, R.; Shimamoto, T.; Ando, J.; Ree, J. Seismic slip record in carbonate-bearing fault zones: An insight from high-velocity friction experiments on siderite gouge. *Geology* **2007**, *35*, 1131–1134. [CrossRef]

113. Verberne, B.A.; de Bresser, J.H.P.; Niemeijer, A.R.; Spiers, C.J.; de Winter, D.A.M.; Plumper, O. Nanocrystalline slip zones in calcite fault gouge show intense crystallographic preferred orientation: Crystal plasticity at sub-seismic slip rates at 18–150 °C. *Geology* **2013**, *41*, 863–866. [CrossRef]
114. Verberne, B.A.; Spiers, C.J.; Niemeijer, A.R.; De Bresser, J.H.P.; De Winter, D.A.M.; Plumper, O. Frictional Properties and Microstructure of Calcite-Rich Fault Gouges Sheared at Sub-Seismic Sliding Velocities. *Pure Appl. Geophys.* **2014**, *171*, 2617–2640. [CrossRef]
115. Spagnuolo, E.; Plumper, O.; Violay, M.; Cavallo, A.; Di Toro, G. Fast-moving dislocations trigger flash weakening in carbonate-bearing faults during earthquakes. *Sci. Rep.* **2015**, *5*, 16112. [CrossRef] [PubMed]
116. Green, H.; Shi, F.; Bozhilov, K.; Xia, G.; Reches, Z. Phase transformation and nanometric flow cause extreme weakening during fault slip. *Nat. Geosci.* **2015**, *8*, U484–U491. [CrossRef]
117. Siman-Tov, S.; Aharonov, E.; Boneh, Y.; Reches, Z. Fault mirrors along carbonate faults: Formation and destruction during shear experiments. *Earth Planet. Sci. Lett.* **2015**, *430*, 367–376. [CrossRef]
118. Delle Piane, C.; Piazolo, S.; Timms, N.; Luzin, V.; Saunders, M.; Bourdet, J.; Giwelli, A.; Ben Clennell, M.; Kong, C.; Rickard, W.; et al. Generation of amorphous carbon and crystallographic texture during low-temperature subseismic slip in calcite fault gouge. *Geology* **2018**, *46*, 163–166. [CrossRef]
119. Mercuri, M.; Scuderi, M.; Tesei, T.; Carminati, E.; Collettini, C. Strength evolution of simulated carbonate-bearing faults: The role of normal stress and slip velocity. *J. Struct. Geol.* **2018**, *109*, 1–9. [CrossRef]
120. Toy, V.; Mitchell, T.; Druiventak, A.; Wirth, R. Crystallographic preferred orientations may develop in nanocrystalline materials on fault planes due to surface energy interactions. *Geochem. Geophys. Geosys.* **2015**, *16*, 2549–2563. [CrossRef]
121. Prior, D.; Boyle, A.; Brenker, F.; Cheadle, M.; Day, A.; Lopez, G.; Peruzzo, L.; Potts, G.; Reddy, S.; Spiess, R.; et al. The application of electron backscatter diffraction and orientation contrast imaging in the SEM to textural problems in rocks. *Am. Mineral.* **1999**, *84*, 1741–1759. [CrossRef]
122. Verberne, B.A.; Chen, J.; Niemeijer, A.R.; de Bresser, J.H.P.; Pennock, G.M.; Drury, M.R.; Spiers, C.J. Microscale cavitation as a mechanism for nucleating earthquakes at the base of the seismogenic zone. *Nat. Commun.* **2017**, *8*. [CrossRef] [PubMed]
123. Pozzi, G.; De Paola, N.; Holdsworth, R.; Bowen, L.; Nielsen, S.; Dempsey, E. Coseismic ultramylonites: An investigation of nanoscale viscous flow and fault weakening during seismic slip. *Earth Planet. Sci. Lett.* **2019**, *516*, 164–175. [CrossRef]
124. Verberne, B.A.; He, C.; Spiers, C.J. Frictional Properties of Sedimentary Rocks and Natural Fault Gouge from the Longmen Shan Fault Zone, Sichuan, China. *Bull. Seismol. Soc. Am.* **2010**, *100*, 2767–2790. [CrossRef]
125. Engelder, J.T. Quartz Fault Gouge: Its Generation and Effect on the Frictional Properties of Sandstone. Ph.D. Thesis, Texas A&M University, College Station, TX, USA, 1973.
126. Viti, C.; Hirose, T. Thermal decomposition of serpentine during coseismic faulting: Nanostructures and mineral reactions. *J. Struct. Geol.* **2010**, *32*, 1476–1484. [CrossRef]
127. Pec, M.; Stünitz, H.; Heilbronner, R.; Drury, M.; de Capitani, C. Origin of pseudotachylites in slow creep experiments. *Earth Planet. Sci. Lett.* **2012**, *355*, 299–310. [CrossRef]
128. Pec, M.; Stünitz, H.; Heilbronner, R.; Drury, M. Semi-brittle flow of granitoid fault rocks in experiments. *J. Geophys. Res. Solid Earth* **2016**, *121*, 1677–1705. [CrossRef]
129. Hadizadeh, J.; Tullis, T.; White, J.; Konkachbaev, A. Shear localization, velocity weakening behavior, and development of cataclastic foliation in experimental granite gouge. *J. Struct. Geol.* **2015**, *71*, 86–99. [CrossRef]
130. Kuo, L.; Song, Y.; Yang, C.; Song, S.; Wang, C.; Dong, J.; Suppe, J.; Shimamoto, T. Ultrafine spherical quartz formation during seismic fault slip: Natural and experimental evidence and its implications. *Tectonophysics* **2015**, *664*, 98–108. [CrossRef]
131. Hayward, K.; Cox, S.; Gerald, J.; Slagmolen, B.; Shaddock, D.; Forsyth, P.; Salmon, M.; Hawkins, R. Mechanical amorphization, flash heating, and frictional melting: Dramatic changes to fault surfaces during the first millisecond of earthquake slip. *Geology* **2016**, *44*, 1043–1046. [CrossRef]
132. Aretusini, S.; Mittempergher, S.; Plumper, O.; Spagnuolo, E.; Gualtieri, A.; Di Toro, G. Production of nanoparticles during experimental deformation of smectite and implications for seismic slip. *Earth Planet. Sci. Lett.* **2017**, *463*, 221–231. [CrossRef]
133. Niemeijer, A. Velocity-dependent slip weakening by the combined operation of pressure solution and foliation development. *Sci. Rep.* **2018**, *8*. [CrossRef] [PubMed]

134. Rowe, C.; Lamothe, K.; Rempe, M.; Andrews, M.; Mitchell, T.; Di Toro, G.; White, J.; Aretusini, S. Earthquake lubrication and healing explained by amorphous nanosilica. *Nat. Commun.* **2019**, *10*. [CrossRef] [PubMed]
135. Fondriest, M.; Smith, S.; Candela, T.; Nielsen, S.; Mair, K.; Di Toro, G. Mirror-like faults and power dissipation during earthquakes. *Geology* **2013**, *41*, 1175–1178. [CrossRef]
136. Tisato, N.; Di Toro, G.; De Rossi, N.; Quaresimin, M.; Candela, T. Experimental investigation of flash weakening in limestone. *J. Struct. Geol.* **2012**, *38*, 183–199. [CrossRef]
137. Chen, X.; Madden, A.; Bickmore, B.; Reches, Z. Dynamic weakening by nanoscale smoothing during high-velocity fault slip. *Geology* **2013**, *41*, 739–742. [CrossRef]
138. Boneh, Y.; Sagy, A.; Reches, Z. Frictional strength and wear-rate of carbonate faults during high-velocity, steady-state sliding. *Earth Planet. Sci. Lett.* **2013**, *381*, 127–137. [CrossRef]
139. Pozzi, G.; De Paola, N.; Nielsen, S.; Holdsworth, R.; Bowen, L. A new interpretation for the nature and significance of mirror-like surfaces in experimental carbonate-hosted seismic faults. *Geology* **2018**, *46*, 583–586. [CrossRef]
140. Verberne, B.A.; Plumper, O.; de Winter, D.A.M.; Spiers, C.J. Superplastic nanofibrous slip zones control seismogenic fault friction. *Science* **2014**, *346*, 1342–1344. [CrossRef]
141. Engelder, J.T. Cataclasis and generation of fault gouge. *Geol. Soc. Am. Bull.* **1974**, *85*, 1515–1522. [CrossRef]
142. Marone, C.; Scholz, C.H. Particle-size distribution and microstructures within simulated fault gouge. *J. Struct. Geol.* **1989**, *11*, 799–814. [CrossRef]
143. Stünitz, H.; Keulen, N.; Hirose, T.; Heilbronner, R. Grain size distribution and microstructures of experimentally sheared granitoid gouge at coseismic slip rates—Criteria to distinguish seismic and aseismic faults? *J. Struct. Geol.* **2010**, *32*, 59–69. [CrossRef]
144. Kendall, K. The impossibility of communiting small particles by compression. *Nature* **1978**, *272*, 710–711. [CrossRef]
145. Karihaloo, B.L. The impossibility of communiting small particles by compression. *Nature* **1979**, *279*, 169–170. [CrossRef]
146. Griffith, A. The phenomena of rupture and flow in solids. *Philos. Trans. R. Soc. Lond.* **1921**, *61*, 163–198. [CrossRef]
147. Sammis, C.; Ben-Zion, Y. Mechanics of grain-size reduction in fault zones. *J. Geophys. Res. Solid Earth* **2008**, *113*. [CrossRef]
148. Tao, N.; Wang, Z.; Tong, W.; Sui, M.; Lu, J.; Lu, K. An investigation of surface nanocrystallization mechanism in Fe induced by surface mechanical attrition treatment. *Acta Mater.* **2002**, *50*, 4603–4616. [CrossRef]
149. Yang, D.; Cizek, P.; Hodgson, P.; Wen, C. Microstructure evolution and nanograin formation during shear localization in cold-rolled titanium. *Acta Mater.* **2010**, *58*, 4536–4548. [CrossRef]
150. Kennedy, L.; White, J. Low-temperature recrystallization in calcite: Mechanisms and consequences. *Geology* **2001**, *29*, 1027–1030. [CrossRef]
151. De Bresser, J.H.P.; Evans, B.; Renner, J. On estimating the strength of calcite rocks under natural conditions. In *Deformation Mechanisms, Rheology and Tectonics: Current Status and Future Perspectives*; De Meer, S., Drury, M.R., de Bresser, J.H.P., Pennock, G.M., Eds.; Geological Society: London, UK, 2002; Volume 200, pp. 309–329.
152. De Bresser, J.H.P.; Spiers, C.J. Strength characteristics of the r, f, and c slip systems in calcite. *Tectonophysics* **1997**, *272*, 1–23. [CrossRef]
153. Wolf, D.; Okamoto, P.R.; Yip, S.; Lutsko, J.F.; Kluge, M. Thermodynamic parallels between solid-state amorphization and melting. *J. Mater. Res.* **1990**, *5*, 286–301. [CrossRef]
154. Oohashi, K.; Hirose, T.; Kobayashi, K.; Shimamoto, T. The occurrence of graphite-bearing fault rocks in the Atotsugawa fault system, Japan: Origins and implications for fault creep. *J. Struct. Geol.* **2012**, *38*, 39–50. [CrossRef]
155. Collettini, C.; Viti, C.; Tesei, T.; Mollo, S. Thermal decomposition along natural carbonate faults during earthquakes. *Geology* **2013**, *41*, 927–930. [CrossRef]
156. Ohl, M.; Plümper, O.; Chatzaras, V.; Wallis, D.; Vollmer, C.; Drury, M. Mechanisms of fault mirror formation in carbonate rocks. *EarthArXiv* **2019**. [CrossRef]
157. Oohashi, K.; Han, R.; Hirose, T.; Shimamoto, T.; Omura, K.; Matsuda, T. Carbon-forming reactions under a reducing atmosphere during seismic fault slip. *Geology* **2014**, *42*, 787–790. [CrossRef]
158. Luque, F.; Pasteris, J.; Wopenka, B.; Rodas, M.; Barrenechea, J. Natural fluid-deposited graphite: Mineralogical characteristics and mechanisms of formation. *Am. J. Sci.* **1998**, *298*, 471–498. [CrossRef]

159. Gao, G.; Mikulski, P.; Harrison, J. Molecular-scale tribology of amorphous carbon coatings: Effects of film thickness, adhesion, and long-range interactions. *J. Am. Chem. Soc.* **2002**, *124*, 7202–7209. [CrossRef]
160. Penn, R.; Banfield, J. Imperfect oriented attachment: Dislocation generation in defect-free nanocrystals. *Science* **1998**, *281*, 969–971. [CrossRef]
161. Niederberger, M.; Colfen, H. Oriented attachment and mesocrystals: Non-classical crystallization mechanisms based on nanoparticle assembly. *Phys. Chem. Chem. Phys.* **2006**, *8*, 3271–3287. [CrossRef]
162. De Yoreo, J.; Gilbert, P.; Sommerdijk, N.; Penn, R.; Whitelam, S.; Joester, D.; Zhang, H.; Rimer, J.; Navrotsky, A.; Banfield, J.; et al. Crystallization by particle attachment in synthetic, biogenic, and geologic environments. *Science* **2015**, *349*. [CrossRef] [PubMed]
163. Gehrke, N.; Colfen, H.; Pinna, N.; Antonietti, M.; Nassif, N. Superstructures of calcium carbonate crystals by oriented attachment. *Cryst. Growth Des.* **2005**, *5*, 1317–1319. [CrossRef]
164. Zhang, H.; Banfield, J. Energy Calculations Predict Nanoparticle Attachment Orientations and Asymmetric Crystal Formation. *J. Phys. Chem. Lett.* **2012**, *3*, 2882–2886. [CrossRef]
165. Zhang, H.; Banfield, J. Interatomic Coulombic interactions as the driving force for oriented attachment. *Crystengcomm* **2014**, *16*, 1568–1578. [CrossRef]
166. De Leeuw, N.; Parker, S. Atomistic simulation of the effect of molecular adsorption of water on the surface structure and energies of calcite surfaces. *J. Chem. Soc. Faraday Trans.* **1997**, *93*, 467–475. [CrossRef]
167. Smith, S.A.F.; Di Toro, G.; Kim, S.; Ree, J.; Nielsen, S.; Billi, A.; Spiess, R. Coseismic recrystallization during shallow earthquake slip. *Geology* **2013**, *41*, 63–66. [CrossRef]
168. Verberne, B.A.; Niemeijer, A.R.; De Bresser, J.H.P.; Spiers, C.J. Mechanical behavior and microstructure of simulated calcite fault gouge sheared at 20–600 °C: Implications for natural faults in limestones. *J. Geophys. Res. Solid Earth* **2015**, *120*, 8169–8196. [CrossRef]
169. Smith, S.A.F.; Nielsen, S.; Di Toro, G. Strain localization and the onset of dynamic weakening in calcite fault gouge. *Earth Planet. Sci. Lett.* **2015**, *413*, 25–36. [CrossRef]
170. Ree, J.; Ando, J.; Han, R.; Shimamoto, T. Coseismic microstructures of experimental fault zones in Carrara marble. *J. Struct. Geol.* **2014**, *66*, 75–83. [CrossRef]
171. Niemeijer, A.; Spiers, C. A microphysical model for strong velocity weakening in phyllosilicate-bearing fault gouges. *J. Geophys. Res. Solid Earth* **2007**, *112*. [CrossRef]
172. Hunfeld, L.; Niemeijer, A.; Spiers, C. Frictional Properties of Simulated Fault Gouges from the Seismogenic Groningen Gas Field Under In Situ P-T -Chemical Conditions. *J. Geophys. Res. Solid Earth* **2017**, *122*, 8969–8989. [CrossRef]
173. Den Hartog, S.; Spiers, C. Influence of subduction zone conditions and gouge composition on frictional slip stability of megathrust faults. *Tectonophysics* **2013**, *600*, 75–90. [CrossRef]
174. Blanpied, M.L.; Lockner, D.A.; Byerlee, J.D. Frictional slip of granite at hydrothermal conditions. *J. Geophys. Res. Solid Earth* **1995**, *100*, 13045–13064. [CrossRef]
175. Chen, J.; Spiers, C. Rate and state frictional and healing behavior of carbonate fault gouge explained using microphysical model. *J. Geophys. Res. Solid Earth* **2016**, *121*, 8642–8665. [CrossRef]
176. Chen, J.; Niemeijer, A.; Spiers, C. Microphysically Derived Expressions for Rate-and-State Friction Parameters, a, b, and D-c. *J. Geophys. Res. Solid Earth* **2017**, *122*, 9627–9657. [CrossRef]
177. Chen, J.; Niemeijer, A. Seismogenic Potential of a Gouge-filled Fault and the Criterion for Its Slip Stability: Constraints FRom a Microphysical Model. *J. Geophys. Res. Solid Earth* **2017**, *122*, 9658–9688. [CrossRef]
178. Van den Ende, M.P.A.; Chen, J.; Ampuero, J.P.; Niemeijer, A.R. A comparison between rate-and-state friction and microphysical models, based on numerical simulations of fault slip. *Tectonophysics* **2018**, *733*, 273–295. [CrossRef]
179. Zhang, X.; Spiers, C.; Peach, C. Compaction creep of wet granular calcite by pressure solution at 28 °C to 150 °C. *J. Geophys. Res. Solid Earth* **2010**, *115*. [CrossRef]
180. Pluymakers, A.M.H.; Spiers, C.J. Compaction creep of simulated anhydrite fault gouge by pressure solution: Theory v. experiments and implications for fault sealing. In *Rock Deformation from Field, Experiments and Theory: A Volume in Honour of Ernie Rutter*; Faulkner, D.R., Mariani, E., Mecklenburgh, J., Eds.; Geological Society, Special Publications: London, UK, 2014; Volume 409.
181. Nakashima, S. Diffusivity of ions in pore water as a quantitative basis for rock deformation estimates. *Tectonophysics* **1995**, *245*, 185–203. [CrossRef]

182. Plummer, L.N.; Busenberg, E. The solubilities of calcite, aragonite and vaterite in CO_2-H_2O solutions between 0 °C and 90 °C, and an evaluation of the aqueous model for the system $CaCO_3$-CO_2-H_2O. *Geochim. Cosmochim. Acta* **1982**, *46*, 1011–1040. [CrossRef]
183. Farver, J.; Yund, R. Volume and grain boundary diffusion of calcium in natural and hot-pressed calcite aggregates. *Contrib. Mineral. Petrol.* **1996**, *123*, 77–91. [CrossRef]
184. Chen, J.; Verberne, B.; Spiers, C. Effects of healing on the seismogenic potential of carbonate fault rocks: Experiments on samples from the Longmenshan Fault, Sichuan, China. *J. Geophys. Res.* **2015**, *120*, 5479–5506. [CrossRef]
185. Chen, J.; Verberne, B.; Spiers, C. Interseismic re-strengthening and stabilization of carbonate faults by "non-Dieterich" healing under hydrothermal conditions. *Earth Planet. Sci. Lett.* **2015**, *423*, 1–12. [CrossRef]
186. Schubnel, A.; Brunet, F.; Hilairet, N.; Gasc, J.; Wang, Y.; Green, H. Deep-Focus Earthquake Analogs Recorded at High Pressure and Temperature in the Laboratory. *Science* **2013**, *341*, 1377–1380. [CrossRef] [PubMed]
187. Bernard, P.; Lyon-Caen, H.; Briole, P.; Deschamps, A.; Boudin, F.; Makropoulos, K.; Papadimitriou, P.; Lemeille, F.; Patau, G.; Billiris, H.; et al. Seismicity, deformation and seismic hazard in the western rift of Corinth: New insights from the Corinth Rift Laboratory (CRL). *Tectonophysics* **2006**, *426*, 7–30. [CrossRef]
188. Valoroso, L.; Chiaraluce, L.; Piccinini, D.; Di Stefano, R.; Schaff, D.; Waldhauser, F. Radiography of a normal fault system by 64,000 high-precision earthquake locations: The 2009 L'Aquila (central Italy) case study. *J. Geophys. Res. -Solid Earth* **2013**, *118*, 1156–1176. [CrossRef]
189. Chiarabba, C.; De Gori, P.; Mele, F. Recent seismicity of Italy: Active tectonics of the central Mediterranean region and seismicity rate changes after the Mw 6.3 L'Aquila earthquake. *Tectonophysics* **2015**, *638*, 82–93. [CrossRef]
190. Fagereng, Å.; Biggs, J. New perspectives on 'geological strain rates' calculated from both naturally deformed and actively deforming rocks. *J. Struct. Geol.* **2018**, in press. [CrossRef]
191. Pfiffner, O.; Ramsay, J. Constraints on geological strain rates—Arguments from finite strain states of naturally deformed rocks. *J. Geophys. Res.* **1982**, *87*, 311–321. [CrossRef]
192. De Bresser, J.H.P.; Ter Heege, J.H.; Spiers, C.J. Grain size reduction by dynamic recrystallization: Can it result in major theological weakening? *Int. J. Earth Sci.* **2001**, *90*, 28–45. [CrossRef]

© 2019 by the authors. Licensee MDPI, Basel, Switzerland. This article is an open access article distributed under the terms and conditions of the Creative Commons Attribution (CC BY) license (http://creativecommons.org/licenses/by/4.0/).